Herschel imaging of 61 Vir: implications for the prevalence of debris in low-mass planetary systems

M. C. Wyatt,[1]* G. Kennedy,[1] B. Sibthorpe,[2] A. Moro-Martín,[3] J.-F. Lestrade,[4]
R. J. Ivison,[2] B. Matthews,[5] S. Udry,[6] J. S. Greaves,[7] P. Kalas,[8,9] S. Lawler,[10]
K. Y. L. Su,[11] G. H. Rieke,[11] M. Booth,[5,12] G. Bryden,[13] J. Horner,[14] J. J. Kavelaars[5]
and D. Wilner[15]

[1]*Institute of Astronomy, University of Cambridge, Madingley Road, Cambridge CB3 0HA*
[2]*UK Astronomy Technology Centre, Royal Observatory, Blackford Hill, Edinburgh EH9 3HJ*
[3]*Centro de Astrobiología (CSIC-INTA), 28850 Torrejón de Ardoz, Madrid, Spain*
[4]*Observatoire de Paris, 77 Avenue Denfert Rochereau, 75014 Paris, France*
[5]*Herzberg Institute of Astrophysics, 5072 West Saanich Road, Victoria, BC V9E 2E7, Canada*
[6]*Observatoire de I'Université de Genève, 51 ch. de Maillettes, CH-1290 Versoix, Switzerland*
[7]*Scottish Universities Physics Alliance, University of St. Andrews, Physics and Astronomy, North Haugh, St Andrews KY16 9SS*
[8]*Department of Astronomy, University of California, 601 Campbell Hall, Berkeley, CA 94720, USA*
[9]*SETI Institute, 515 North Whisman Road, Mountain View, CA 94043, USA*
[10]*Department of Physics and Astronomy, University of British Columbia, 6244 Agricultural Road, Vancouver, BC V6T 1Z1, Canada*
[11]*Steward Observatory, University of Arizona, Tucson, AZ 85721, USA*
[12]*Department of Physics and Astronomy, University of Victoria, Elliott Building, 3800 Finnerty Road, Victoria, BC V8P 5C2, Canada*
[13]*Jet Propulsion Laboratory, California Institute of Technology, 4800 Oak Grove Drive, Pasadena, CA 91109, USA*
[14]*Department of Astrophysics and Optics, School of Physics, University of New South Wales, Sydney 2052, Australia*
[15]*Harvard-Smithsonian Center for Astrophysics, 60 Garden Street, Cambridge, MA 02138, USA*

ABSTRACT

This paper describes *Herschel* observations of the nearby (8.5 pc) G5V multi-exoplanet host star 61 Vir at 70, 100, 160, 250, 350 and 500 μm carried out as part of the DEBRIS survey. These observations reveal emission that is significantly extended out to a distance of >15 arcsec with a morphology that can be fitted by a nearly edge-on (77° inclination) radially broad (from 30 au out to at least 100 au) debris disc of fractional luminosity 2.7×10^{-5}, with two additional (presumably unrelated) sources nearby that become more prominent at longer wavelengths. Chance alignment with a background object seen at 1.4 GHz provides potential for confusion, however, the star's 1.4 arcsec yr^{-1} proper motion allows archival *Spitzer* 70 μm images to confirm that what we are interpreting as *disc* emission really is circumstellar. Although the exact shape of the disc's inner edge is not well constrained, the region inside 30 au must be significantly depleted in planetesimals. This is readily explained if there are additional planets outside those already known (i.e. in the 0.5–30 au region), but is also consistent with collisional erosion. We also find tentative evidence that the presence of detectable debris around nearby stars correlates with the presence of the lowest mass planets that are detectable in current radial velocity surveys. Out of an unbiased sample of the nearest 60 G stars, 11 are known to have planets, of which six (including 61 Vir) have planets that are all less massive than Saturn, and four of these have evidence for debris. The debris towards one of these planet hosts (HD 20794) is reported here for the first time. This fraction (4/6) is higher than that expected for nearby field stars (15 per cent), and implies that systems that form low-mass planets are also able to retain bright debris discs. We suggest that this correlation could arise because such planetary

*E-mail: wyatt@ast.cam.ac.uk

systems are dynamically stable and include regions that are populated with planetesimals in the formation process where the planetesimals can remain unperturbed over Gyr time-scales.

Key words: planets and satellites: formation – planet–disc interactions – circumstellar matter – planetary systems.

1 INTRODUCTION

Main-sequence stars, like the Sun, are often found to be orbited by circumstellar material that can be categorized into two groups, planets and debris, the latter of which is composed of asteroids, comets and the dust derived from them (e.g. Wyatt 2008; Krivov 2010). Although there are 11 examples of nearby stars that are known to have both planets and debris (e.g. Moro-Martín et al. 2010), there is as yet no evidence for any correlation between the two types of material (Greaves et al. 2004; Kóspál et al. 2009), and the properties of the debris discs around stars that have planets are not found to be significantly different to those of stars without known planets (Bryden et al. 2009). This is usually explained as a consequence of the spatial separation between the planets (which are typically found within a few au) and debris (which is typically found at 10s of au).

Despite this spatial separation, it is still expected that outer debris can be affected by the gravitational perturbations of close-in planets (Mustill & Wyatt 2009), and that such debris can have a significant dynamical effect on the evolution of interior planets, e.g. through promoting migration (Kirsh et al. 2009) or by triggering instabilities (Tsiganis et al. 2005; Levison et al. 2011). The delivery of debris to the inner planets may also be an important source of volatiles to the planets (e.g. Horner & Jones 2010). Furthermore, it is reasonable to expect that the initial conditions in protoplanetary discs that favour the formation of certain types of inner planetary system might also result in (or exclude) specific types of debris disc (e.g. Wyatt, Clarke & Greaves 2007c; Raymond et al. 2012). Thus the search for any correlation between the two phenomena continues (e.g. Maldonado et al. 2012), so that light may be shed on the interaction between planets and debris, as well as on the formation mechanism for the two components.

This paper describes observations carried out as part of the key programme Disc Emission via a Bias-free Reconnaissance in the Infrared/Submillimetre (DEBRIS) on the *Herschel Space Observatory*[1] (Pilbratt et al. 2010). DEBRIS is an unbiased survey searching for evidence of circumstellar dust at 100 and 160 μm towards the nearest ∼80 stars of each spectral type A, F, G, K and M (see Phillips et al. 2010, for a description of the sample). The first results have already shown that *Herschel* observations have the potential to detect discs down to much fainter levels than previous observations, and moreover have the resolution to resolve the discs at far-infrared (IR) wavelengths (Matthews et al. 2010; Churcher et al. 2011; Kennedy et al. 2012).

Several of the stars in the sample are known planet hosts; others may be found to host planets in the future. As such, the survey is ideally suited to determining whether any correlation exists between planets and debris. Here we focus on *Herschel* observations of the star 61 Vir (HD 115617), which is a main-sequence G5

star. At 8.55 ± 0.02 pc (van Leeuwen 2007) 61 Vir is the eighth nearest main-sequence G star to the Sun. This star exemplifies the merits of an unbiased survey, since the star was relatively unremarkable at the time the survey was conceived, but has since been found by radial velocity surveys to host three planets at 0.05, 0.218 and 0.478 au with minimum masses (i.e. $M_{pl} \sin i$) of 5.1, 18.2 and 22.9 $M_\oplus$, respectively (Vogt et al. 2010), and has subsequently been the subject of several studies on the secular dynamics of its planetary system (Batygin & Laughlin 2011; Greenberg & van Laerhoven 2012) and on its formation mechanism (Hansen & Murray 2012).

Thus 61 Vir is one of the first of a growing number of systems around which only low-mass planets are known, which we define here as sub-Saturn mass. Such low-mass planets have only been discovered recently, often in multiple planet systems, either by high precision radial velocity measurements (Lovis et al. 2006; Mayor et al. 2011), or by transiting studies with *Kepler* (Borucki et al. 2011; Lissauer et al. 2011).

Previous *Spitzer* observations showed that 61 Vir hosts a debris disc with a fractional luminosity of around 2×10^{-5} (Bryden et al. 2006), but the location of the emission was uncertain, with estimates ranging from 8.3 au (Trilling et al. 2008) and 4–25 au (Lawler et al. 2009) to 96–195 au (Tanner et al. 2009). Our observations confirm the existence of a bright debris disc, and moreover the resolution of the images permits the disc structure to be ascertained. This allows us to consider the relationship between the disc and the planetary system, and the implications for the system's formation and evolution. Given that there are other systems with debris in low-mass planetary systems (e.g. Beichman et al. 2011), we also consider whether this discovery heralds an emerging correlation between the presence of debris and low-mass planets (e.g. as predicted by Raymond et al. 2011).

The layout of the paper is as follows. The observations are described in Section 2, including both the *Herschel* observations and archival *Spitzer* and radio observations that are needed to disentangle circumstellar from extragalactic emission. Modelling of the *Herschel* observations is presented in Section 3 to derive the radial distribution of dust. We find that the known planets probably do not play a primary role in stirring the debris, and discuss the implications of the debris for the evolution of the planetary system in Section 4. Finally a statistical analysis of an unbiased sample of nearby stars is given in Section 5 to consider the possibility of a disc–planet correlation. Conclusions are presented in Section 6.

2 OBSERVATIONS

2.1 *Herschel*

2.1.1 PACS

Herschel DEBRIS observations of 61 Vir were taken on 2010 August 10. These consist of simultaneous 100 and 160 μm images taken with Photodetector and Array Camera and Spectrometer (PACS; Poglitsch et al. 2010), using the small scan-map mode.

Table 1. *Herschel* observations of 61 Vir.

ObsId	Date	Instrument	Duration (s)
1342202551	2010 August 10	PACS 100/160	445
1342202552	2010 August 10	PACS 100/160	445
1342212412	2011 January 9	SPIRE 250/350/500	721
1342223608	2011 July 3	PACS 70/160	445
1342223609	2011 July 3	PACS 70/160	445

Scan-map observations have eight repeats in two scan directions that differ by $40°$, at a scan rate of 20 arcsec s^{-1}. Eight 3 arcmin scan legs were performed per map with a 2 arcsec separation between legs. The total observing time was 890 s. An identical observation was obtained on 2011 July 3, this time with simultaneous 70 and 160 μm images. The *Herschel* observations are summarized in Table 1.

The data were reduced using a near-standard pipeline with the *Herschel* Interactive Processing Environment (HIPE, version 7.0 build 1931; Ott 2010). The data were pre-filtered to remove low-frequency noise using a boxcar filter with a width of 66 arcsec at 70 and 100 μm and 102 arcsec at 160 μm. Different filter widths were tested to confirm that this did not significantly affect conclusions about disc fluxes or morphology. The point spread function (PSF) of the PACS instrument includes power on large scales (e.g. 10 per cent beyond 1 arcmin) that is removed by the filtering process. For point sources this can be readily accounted for in the calibration by comparison of the aperture fluxes of bright stars with known fluxes.

For extended sources like 61 Vir, the calibration is slightly more complicated, as described below.

The pixel scale in the maps was set to 1 arcsec at 70 and 100 μm and 2 arcsec at 160 μm. Since this is smaller than the native pixel scale, noise in neighbouring pixels is correlated, and to derive the uncertainty on any given measurement (such as flux within an aperture) the noise per pixel in the resulting map must be interpreted appropriately (Fruchter & Hook 2002; Kennedy et al. 2012). Because the DEBRIS survey comprises many stars, we can confirm that this correction has been applied correctly, because a histogram of (observed–predicted)/uncertainty for all observations is consistent with a Gaussian of unity dispersion as expected. If the histogram had been wider, for example, it would indicate that the uncertainties had been underestimated.

Fig. 1 shows the 70, 100 and 160 μm images cropped to the region $±40$ arcsec from the star. The peak emission at 70 and 100 μm was found, respectively, to be offset (in different directions) by 1.8 and 1.6 arcsec from the nominal location of the star ($13^h18^m23^s.52$, $-18°18'51''.6$). Since this is consistent with the expected pointing uncertainty of *Herschel* of 2 arcsec (1σ), a value that in turn is consistent with the pointing offsets seen for stars detected in the DEBRIS sample, we applied a pointing correction on the assumption that the star was at this peak location. As the two 160 μm images were taken simultaneously with those at 70 and 100 μm, this re-registering process also determines the centre of the 160 μm maps that were then co-added to give the presented image.
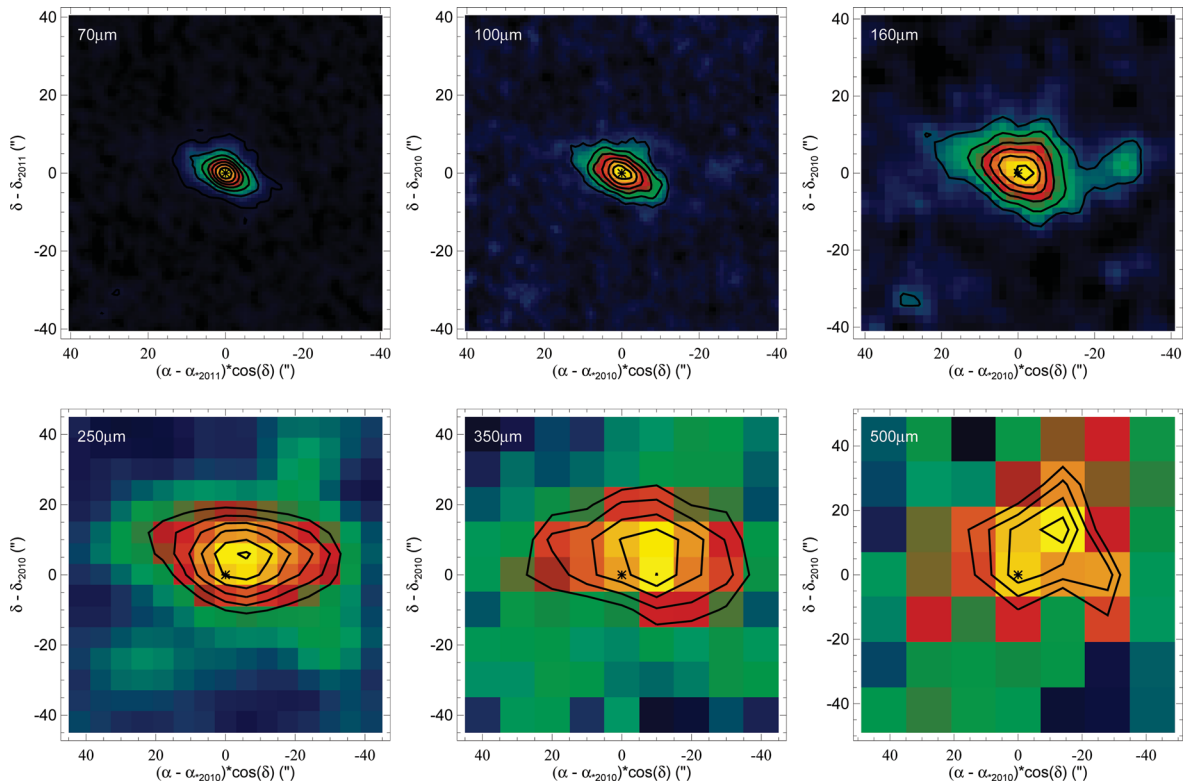

Figure 1. DEBRIS PACS and SPIRE images of 61 Vir, all centred on the star at the epoch of the observation, the location of which is shown with an asterisk: top left – 70 μm; top middle – 100 μm; top right – 160 μm; bottom left – 250 μm; bottom middle – 350 μm and bottom right – 500 μm. Contours shown in black are those of the presented images at levels of 4, 13, 22, 31, 40, 49, 58 times $\sigma_{70} = 0.028$ mJy pixel^{-1} at 70 μm; 4, 9, 14, 19, 24, 29 times $\sigma_{100} = 0.029$ mJy pixel^{-1} at 100 μm; 4, 8, 12, 16, 20, 24 times $\sigma_{160} = 0.052$ mJy pixel^{-1} at 160 μm; 3, 4, 5, 6, 7, 8 times $\sigma_{250} = 4.8$ mJy beam^{-1} at 250 μm; 2, 3, 4, 5, 6 times $\sigma_{350} = 6.2$ mJy beam^{-1} at 350 μm and 2, 2.5, 3, 3.5 times $\sigma_{500} = 6.4$ mJy beam^{-1} at 500 μm, where σ_λ is the pixel-to-pixel uncertainty in the images (which is measured from the images and so includes confusion noise), and the colour scale goes from $-2\sigma_\lambda$ to the maximum brightness.
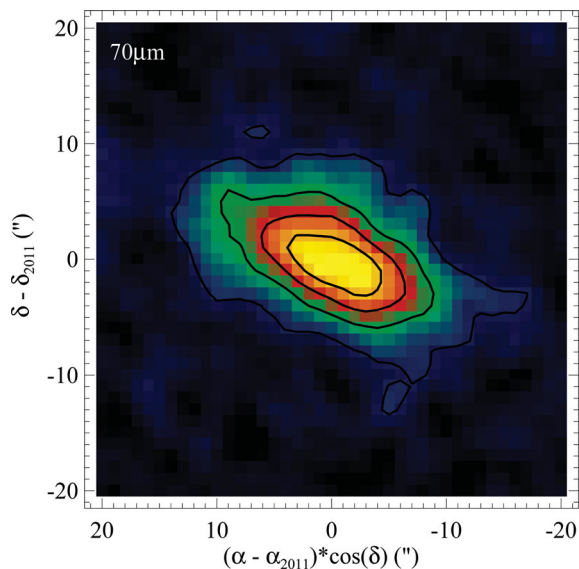
Figure 2. Star-subtracted 70 μm PACS image of 61 Vir. Contours are the same as in Fig. 1.

The images at all three PACS wavelengths show a very similar morphology, of emission that is peaked on the star, but that is extended symmetrically about the star along a position angle (PA) of ~65°. This suggests that the star is surrounded by a disc that is inclined to our line of sight. After subtracting a PSF scaled to the stellar photospheric emission (see Fig. 2 for the resulting image at 70 μm), elliptical Gaussian fits to the three images find for the full width at half-maximum (FWHM) of the major and minor axes and for the PA: 15.9 ± 0.36, 7.7 ± 0.2 arcsec, $64° \pm 1.3°$ at 70 μm; 17.4 ± 0.7, 8.7 ± 0.3 arcsec, $65° \pm 1.6°$ at 100 μm and 24.8 ± 2, 14.8 ± 1 arcsec, $75° \pm 4.5°$ at 160 μm. Given that the FWHM of the PSF is 5.6, 6.7 and 11.4 arcsec at these wavelengths, the emission is extended along both the major and the minor axes. Quadratic subtraction of the FWHM of the PSF suggests a disc inclination of around $20° \pm 2°$ from edge-on at 70 and 100 μm and $26° \pm 7°$ at 160 μm (see Section 4.2 for a discussion of the implications for the planet masses); the fact that the long wavelength emission is more extended (after this quadratic subtraction) than that at 70 and 100 μm suggests that the disc may be radially broad (since longer wavelengths tend to probe cooler material). The uncertainty in the level of photospheric emission to be subtracted from the images has a negligible effect on the inferred disc structure; e.g. the resulting uncertainties in the parameters of the elliptical Gaussian fit are smaller than those quoted above.

The total fluxes were calculated from the images using aperture photometry. A circular 20 arcsec (170 au) radius aperture was employed since, at least for 70 and 100 μm, it was found that there was no flux present on larger scales. The fluxes derived in this way need to be revised because a significant fraction of the flux has been filtered out in the reconstruction of the map. This correction factor has been derived for point sources in the DEBRIS survey to be 16, 19, 21 per cent at 70, 100 and 160 μm, respectively, based on how the inferred fluxes compare with those predicted from the photosphere models for those stars for which purely photospheric emission is confidently detected, and we consider the uncertainty in our correction factor to be ~5 per cent (i.e. the correction factor at 70 μm is 16 ± 5 per cent). These values are consistent with the aperture

correction for a 20 arcsec aperture quoted by the PACS team[2] of 17, 20 and 26 per cent. Although this correction factor was derived for point sources, it should also apply to resolved sources, as long as the aperture size is larger than the extended source, a condition that is tested for the 61 Vir maps in Section 3. The derived fluxes are 198 ± 3 mJy at 70 μm, 152 ± 6 mJy at 100 μm and 133 ± 6 mJy at 160 μm (noting that these uncertainties need to be increased due to the systematic effects outlined in the next paragraph).

The uncertainties in the previous paragraph have been derived from the distribution of fluxes obtained by placing apertures of the same size at different locations in the map. Given the uneven coverage of the map resulting from the observing strategy, the centres of these apertures were constrained to lie in regions with uncertainties within 10 per cent of that of the region around 61 Vir. Additional uncertainties of 1.4, 1.6 and 3.5 per cent for repeatability in the different wavebands,[3] and the 5 per cent calibration uncertainty mentioned above, also need to be applied. A quadratic combination of uncertainties results in ± 11, ± 10 and ± 17 mJy at 70, 100 and 160 μm, respectively.

These fluxes can be compared with those determined by Multiband Imaging Photometer for *Spitzer* (MIPS). The 70 μm MIPS bandpass is very similar to that of PACS, and the MIPS flux has been quoted as 185.6 ± 16.6 (Bryden et al. 2006) and 195 ± 8 mJy (Trilling et al. 2008), but since the source is resolved the flux is expected to be higher than early estimates, with 224 ± 8 mJy quoted most recently (Lawler et al. 2009). In Section 2.2.2 we reanalyse the MIPS data to give 237 ± 10 mJy in a 36 arcsec radius aperture. Although the PACS flux is lower than that measured by MIPS, the values are consistent within plausible statistical and systematic errors (e.g. cross-calibration between the instruments). The 160 μm MIPS flux is given as between 89 and 141 ± 20 mJy (Tanner et al. 2009), where different values are obtained depending on how the observations are corrected for a spectral leak. These fluxes are very close to that measured by PACS, and given the issues with the leak, the MIPS flux is not used in the subsequent analysis.

There are two additional lower level features in the PACS images. There is clearly a source offset ~27 arcsec to the west of the star. This is not detected at 70 μm (a 3σ upper limit of 6 mJy), it is present above the 3σ level at 100 μm (flux of 10 ± 2 mJy) and is more confidently detected at 160 μm (flux of 19 ± 2 mJy). Given the low signal-to-noise ratio, there is no evidence that this emission is extended, and we attribute it to a background source. There is also a protrusion to the north of the star which occurs in the 4σ contour at 70 and 100 μm, and in the 12σ contour at 160 μm. For the shorter wavelengths this level of perturbation is consistent with that expected from noise superimposed on a symmetrical disc, but the deviation at 160 μm cannot be explained in this way. We considered whether this is caused by the shape of the PACS beam, which at such low levels is tri-lobed (noting that the telescope PAs for the two 160 μm images differ by just 6° and so the PSF for the combined image is still tri-lobed). However, preliminary modelling showed that an asymmetry of this magnitude could not be caused by the beam shape, and we concluded that this is a real feature that originates either in a background source, or in a cold spot in the disc. The presence of such an extra component explains why the elliptical Gaussian fitting resulted in a higher inferred inclination from the 160 μm image (26°) than at shorter wavelengths (20°).

2.1.2 SPIRE

Follow-up observations were obtained on 2011 January 9 with Spectral and Photometric Imaging Receiver (SPIRE; Griffin et al. 2010) using small-map mode, resulting in simultaneous 250, 350 and 500 μm images (see Table 1). The data were reduced using HIPE (version 7.0 build 1931), adopting the natural pixel scale of 6, 10 and 14 arcsec at 250, 350 and 500 μm, respectively; the beam size at these wavelengths is 18.2, 24.9 and 36.3 arcsec. The resulting images are shown in Fig. 1.

Emission is confidently detected at 250 and 350 μm in the vicinity of the star, and is also found to be extended beyond the beam at these wavelengths. Surprisingly though, the emission is extended along a different PA to the extension seen by PACS, and furthermore the peak is found to be offset significantly (∼7 arcsec) from the star (see Fig. 1). For example, a 2D Gaussian fit to the 250 and 350 μm images finds FWHM for the major and minor axes and PAs and centres of 43, 22 arcsec and 82°, at (5.7 arcsec east, 4.9 arcsec north), and 48, 28 arcsec and 85°, at (6.9 arcsec east, 5.3 arcsec north).

Since the pointing accuracy of *Herschel* is still 2 arcsec for the SPIRE observations, such a large offset is highly unlikely to be caused by a pointing error. Rather we prefer to attribute the observed morphology, both the offset centre and the different PA, to the superposition of emission from at least two sources. That is, the circumstellar component seen at all PACS wavelengths and the background source 27 arcsec west of 61 Vir seen most prominently at 160 μm with a spectrum rising towards longer wavelengths, and probably also a source to the north of the star. This superposition is illustrated in Fig. 3 (left).

This superposition makes it problematic to derive fluxes for the circumstellar component at SPIRE wavelengths. In this section we present total fluxes measured within apertures large enough to encompass the emission from both sources, noting that a significant fraction of this is expected to arise from the background object(s). Within a 40 arcsec radius aperture, the emission at 250, 350 and 500 μm is 120 ± 21, 55 ± 17 and 20 ± 12 mJy. Again, these uncertainties have to be enhanced by a 7 per cent repeatability and calibration uncertainty (see SPIRE observer's manual). In Section 3

an alternative approach is used to separate the flux from the different components by modelling the image as a circumstellar disc with offset point sources.

2.2 Ancillary data

2.2.1 VLA

To assess the possibility that there is extragalactic emission in the vicinity of 61 Vir we searched the literature for previous radio observations. Very Large Array (VLA) observations on 1995 January 15 taken as part of the NRAO VLA Sky Survey (Condon et al. 1998) detected a 50.9 ± 1.9 mJy source at 1.4 GHz at a location ($13^h18^m23^s22$, $-18°18'51''9$), with positional uncertainty of ∼1 arcsec. This source was noted to be extended beyond the 45 arcsec beam, with a fitted (deconvolved) FWHM of 33.2 ± 2.0 arcsec along a major axis at a PA of $3°7 ± 2°4$ (compared with a FWHM of <18.4 arcsec along the minor axis).

A search of the VLA archive found a 5 GHz scan of the region dating back to 1987 February 24 with ∼10 arcsec resolution (in DnC configuration). These data, imaged using uniform weighting (robust = −5), are shown in Fig. 3 (middle) indicating a double-lobed structure. Fitting this as two Gaussians gives 8.0 mJy for the southerly lobe ($13^h18^m23^s14$, $-18°19'04''7$) and 8.8 mJy for the northerly lobe ($13^h18^m23^s13$, $-18°18'39''3$), both of which have deconvolved sizes of around $7 × 4$ arcsec^2; similar results are obtained from images reduced with natural weighting. The peak of the 1.4 GHz emission lies, to within the pointing uncertainty, directly between the lobes.

At the epoch of the first (5 GHz) radio observations the star was offset ∼39 arcsec north-east of the centre of the radio emission. The high proper motion of 61 Vir, −1.07 arcsec yr^{-1} in RA and −1.06 arcsec yr^{-1} in Dec., means that the star had moved 11.9 arcsec to the south-west by the time of the second (1.4 GHz) radio observations. Thus the lack of change in the centroid of the radio emission from 1987 to 1995 implies that the radio emission was not comoving with the star (see Fig. 3); it can thus be assumed to be a background object. Indeed, the morphology and spectral index of the radio
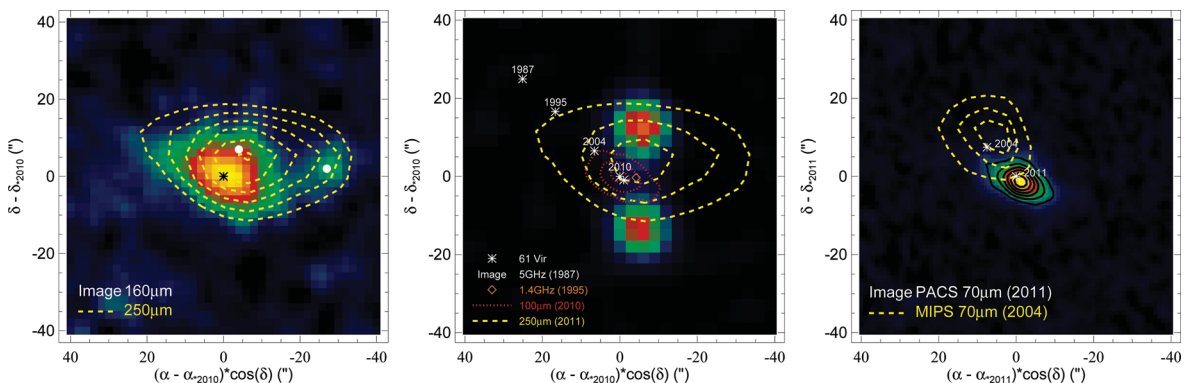

Figure 3. Disentangling the confusion towards 61 Vir. Left: superposition of the 250 μm contours on to the 160 μm image suggests that the 250 μm morphology is composed of a circumstellar component (centred on the asterisk) and two offset sources (centred on the white dots). Middle: the high proper motion of 61 Vir (see asterisks for the location of the star at the different observed epochs) confirms that double-lobed radio emission that is centred just 5 arcsec from 61 Vir at the epoch of the *Herschel* observations is background and not comoving with the star. The presented image shows 5 GHz observations from 1987, and the brown diamond shows the centroid of an extended 1.4 GHz source detected in 1995. Right: the high proper motion of 61 Vir confirms that the extension of the 70 μm emission seen in 2011 with PACS (image reproduced from Fig. 1) was also seen in the archival *Spitzer* MIPS 70 μm image from 2004, which is shown with yellow contours at 50, 75 and 90 per cent of the peak value at 6.84 mJy pixel^{-1}. The high proper motion of the star confirms that this extension is comoving with the star, and so validates the circumstellar interpretation for the majority of the emission seen at 70–160 μm.

emission are typical for a non-thermal jet, which most likely originates from an active galactic nucleus (AGN; Condon et al. 1998) that is directly between the lobes.

The stellar proper motion has the unfortunate consequence that the star's location at the epoch of the *Herschel* observations (see Section 2.1.1) was just ~4 arcsec east of the putative AGN. Thus it must be considered whether the emission seen with *Herschel* is associated with the extragalactic radio emission rather than being circumstellar. It is not possible to predict the far-IR brightness of the extragalactic emission from its radio flux, since the far-IR/radio correlation does not hold for radio-loud AGN.

2.2.2 MIPS

The possibility that the emission interpreted as circumstellar is in fact a background object is ruled out by archival MIPS observations taken at both 24 and 70 μm on 2004 June 21, that we have re-reduced here using an updated pipeline. Since the star contributes the majority of the 24 μm emission, this image does not provide information on the morphology of any circumstellar emission. However, the 70 μm image can be compared directly with that obtained at the same wavelength with *Herschel* 7 yr later.

The MIPS 70 μm observation has lower resolution (FWHM of 19 arcsec) than that of PACS (FWHM of 5.6 arcsec), but the MIPS contours (e.g. those shown in Fig. 3, right) are significantly extended beyond the beam, a point already noted in Lawler et al. (2009). Both 70 μm images include the flux from the point-like star, though at 48.5 mJy this contributes only around 20 per cent of the total emission, and the morphology seen by MIPS does not readily identify this as a distinct component as does the higher resolution PACS image. However, the MIPS 70 μm emission is seen to be extended along a PA that is very similar to that seen in the PACS images, i.e. $56° \pm 5°$, with a 2D Gaussian resulting in FWHM of 24.5 ± 0.6 and 20.8 ± 0.5 arcsec along the major and minor axes, respectively.

As previously noted the *Herschel* pointing accuracy is 2 arcsec; to allow a proper comparison, the astrometry of the PACS image in Fig. 3 (right) is that given by the *Herschel* pointing (i.e. the small correction used to recentre the image in Fig. 1 has not been applied). The pointing accuracy of *Spitzer*[4] is 1 arcsec, and again this has not been corrected for in Fig. 3 (right), explaining the 2.7 arcsec offset of the peak from the stellar location at this epoch. We conclude that the stellar proper motion allows us to confirm that the excess emission is centred on the star, and that both epochs see the same emission morphology that is comoving with the star; i.e. it is not possible to interpret this emission as a stationary background object.

Given the lower resolution of the *Spitzer* beam, the MIPS 70 μm image is not used in subsequent modelling of the dust distribution, although the total flux derived from the image using a 36 arcsec radius aperture was reported in Section 2.1.1 as 237 ± 10 mJy, where it was compared with that derived from PACS. Virtually all the flux at this wavelength is within 20 arcsec radius, since smaller aperture radii measure 223 mJy (16 arcsec radius) and 233 mJy in (20 arcsec radius).

Photometry on the 24 μm image was used in the spectral energy distribution (SED) modelling. The total flux derived from fitting a PSF to the 24 μm image is 457.8 ± 4.6 mJy, compared with a

stellar flux of 441.4 ± 8 mJy, with no evidence for extension beyond the 5.5 arcsec beam. Thus this re-reduction has resulted in a modest upwards revision of the flux from the ~450 mJy reported previously (Bryden et al. 2006; Trilling et al. 2008), and consequently there is now marginal evidence, taking uncertainties in the photospheric contribution into account, for a small ~1.8σ excess at this wavelength. This flux is consistent with that seen at 24 μm by Infrared Spectrograph (IRS; see Section 3.2 and Fig. 5). There is no evidence for any flux at the location of the putative AGN, which was 13 arcsec from the star at the time of the observations; isolated point sources above 0.51 mJy could have been detected in the MIPS image with >3σ confidence, but given its proximity to the star the limit on the 24 μm AGN flux is ~5 times higher.

2.2.3 STIS

Archival *Hubble Space Telescope* (*HST*)/Space Telescope Imaging Spectrograph (STIS) images were searched for evidence either for scattered light from the debris disc or for extragalactic emission. The data were obtained as part of a calibration programme (CAL/STIS-8419, PI Charles Proffitt), and were not optimized for a debris disc search. For example, images were obtained with a 1100×588 pixel subarray (5.58×2.98 arcsec^2) and contemporaneous images for the subtraction of the PSF were not obtained. 61 Vir was observed on 2000 March 11 and again on 2000 May 14. In both observations 61 Vir was occulted at two positions behind a tapered focal plane occulting wedge. At the first position the wedge is 1.0 arcsec wide, and 160 frames with 7 s integration each were obtained. At the second position the wedge is 1.8 arcsec wide, and 56 frames of 7 s each were acquired. The only difference between the two epochs of observation, aside from wedge width and total exposure time, is that in 2000 March 11 the telescope was oriented such that north is $102°.44$ counterclockwise from the $+Y$-axis of the detector, whereas in 2000 May 14 north is $51°.19$ clockwise from the $+Y$-axis. For PSF subtraction we registered the two epochs of data (for a given wedge position) and subtracted 61 Vir from itself. The difference in telescope PA means that a linear feature symmetric about the star, such as a debris disc midplane, would be offset from itself by $26°.4$.

Fig. 4 shows our PSF-subtracted image with 61 Vir occulted behind the 1.8 arcsec wide occulting wedge position. Nebulosity from circumstellar dust is not detected. The observations made with the 1.0 arcsec wide occulting wedge position are more sensitive closer to the star, and from these we estimate an approximate 3σ sensitivity for an extended source at 3.7 arcsec radius of 20.0 mag arcsec^{-2} in the Vega mag *V* band. At radii $\geq$10 arcsec the data for both occulting wedges have an approximate 3σ limiting sensitivity of 21.5 mag arcsec^{-2}. When combined with the far-IR images, these limits set useful constraints on the albedos of the dust grains in the disc that are discussed in Sections 3.3.1, 3.3.2 and 3.3.3. Unfortunately, given the epoch of the STIS observations, the field of view does not encompass the possible extragalactic source that is currently west of 61 Vir.

3 MODELLING

Here we consider the structure of the disc required to explain both the images presented in Section 2, and the spectrum of the disc emission. To do so, first the spectrum of the star is determined (Section 3.1), then additional data needed to constrain the shape

---

[4] http://irsa.ipac.caltech.edu/data/SPITZER/docs/spitzermission/missionoverview/spitzertelescopehandbook/12/
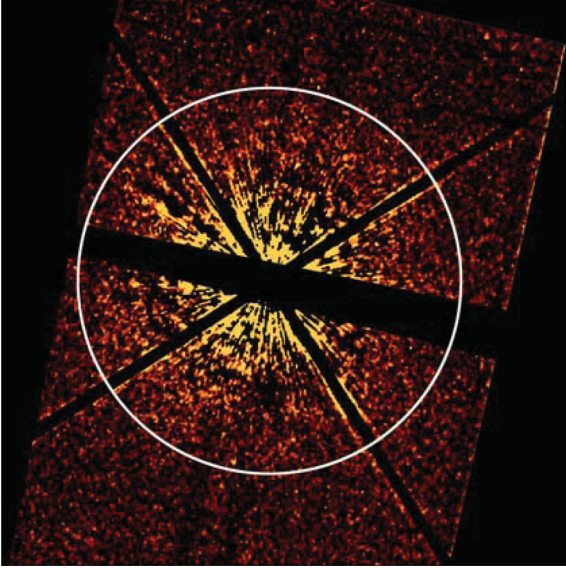
Figure 4. *HST*/STIS optical image of 61 Vir. North is up, east is left, and the white circle indicates 10 arcsec radius. We show the data with a 3 × 3 pixel median filter to improve sensitivity to faint extended sources. A software mask blocks orthogonal diffraction spikes and the occulting bar that differs from a horizontal orientation by 12°. With a PA of 65°, the midplane of the 61 Vir debris disc is offset from the bar by another 13° clockwise, but is not detected in this image.

of the disc's emission spectrum is described (Section 3.2), before modelling of all the observational data is undertaken in Section 3.3.

3.1 The star

The main-sequence G5 star 61 Vir has an age estimated as 4.6 ± 0.9 Gyr using gyrochronology (Wright et al. 2011; Vican 2012), a mass of 0.88 $M_{\odot}$ and a metallicity of [Fe/H] = −0.02 ± 0.01 (Sousa et al. 2008). Its spectrum was determined by fitting PHOENIX models from the *Gaia* grid (Brott & Hauschildt 2005; Hauschildt & Baron 2009) to the observational data available for the star at wavelengths shorter than 12 μm where we can be confident that there is minimal contribution from the disc. This fit includes fluxes from Tycho-2 (B_T, V_T), Two Micron All Sky Survey (2MASS; *J*, *H*, K_s), *AKARI* (9 μm), *IRAS* (12 μm) (see Kennedy et al. 2012 for more details on this procedure).

A best fit was found with $T_{\mathrm{eff}} = 5602$ K scaled to a luminosity of 0.84 $L_{\odot}$. Photospheric fluxes based on this model have a 1σ uncertainty of ±2 per cent. The same process was applied to other stars from the DEBRIS survey (Kennedy et al. 2012), and a comparison of the predicted fluxes to those observed at longer wavelengths for stars where a disc is not present provides confidence that this uncertainty is reasonable. The predicted stellar spectrum is shown in blue on Fig. 5, and fluxes predicted in the *Herschel* bands, with no colour correction, are 50.9, 25.1, 10.0, 4.0, 2.0 and 1.0 mJy at 70, 100, 160, 250, 350 and 500 μm, respectively, while for MIPS 24 μm the stellar flux is predicted at 441.4 mJy.

3.2 Excess spectrum

The spectrum of the excess (i.e. the observed flux less than expected from the photosphere) is plotted in Fig. 5. In addition to the fluxes from Section 2, this plot includes the *IRAS* 60 μm flux measured
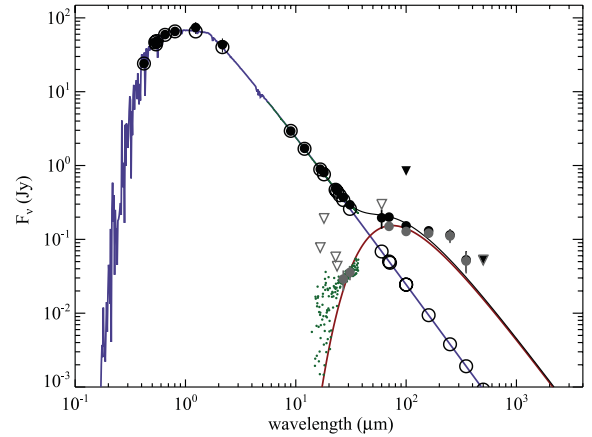

Figure 5. SED of 61 Vir. Total fluxes are black circles, open circles are predicted photospheric fluxes and grey circles are photosphere subtracted (i.e. excess) fluxes; upper limits are plotted as downward pointing triangles (grey and open for excess fluxes and black and solid for total fluxes). Data points from the pre-binned IRS spectrum are shown in green beyond 10 μm. The photospheric model is shown with a blue line, and is a fit to data <12 μm. The longer wavelength excess fluxes are fitted as a 68 K blackbody of fractional luminosity 2.7 × 10^{-5} that is shown in red. The total flux from the models (photosphere plus blackbody) is shown with a black solid line.

using SCANPI[5] of 210 ± 60 mJy, and importantly also includes the *Spitzer* IRS spectrum (AOR 15998976) that was first presented in Lawler et al. (2009). Here we use the more recent the Cornell Atlas of *Spitzer*/IRS Sources (CASSIS) reduction (Lebouteiller et al. 2011), except that the spectra from the individual modules were aligned and then the whole spectrum was scaled so that the flux in the 8–9 μm range matched that of our model stellar spectrum (Section 3.1). This is because the 8 per cent calibration accuracy of IRS (Lawler et al. 2009) is lower than that of our photospheric model, and the shape of the IRS spectrum indicates that there is no contribution from the disc at such wavelengths (e.g. Lawler et al. 2009 report an excess of −3.6 ± 1.4 mJy from the 8.5–12 μm range). To aid the modelling, the IRS spectrum was averaged over seven bins 2–4 μm wide, with the uncertainty in the measurement taken from the distribution of measurements within that bin summed quadratically with the 2 per cent calibration uncertainty of the spectrum (Beichman et al. 2006). For example, this process finds a flux of 270 ± 10 mJy in the range 30–34 μm, which is 24.4 mJy higher than the predicted photospheric flux, and can be compared with a 30.8 ± 2.0 mJy excess reported in Lawler et al. (2009).

The overall shape of the excess spectrum resembles that of a blackbody. Indeed the whole spectrum can be fitted reasonably well by a single temperature at 68 K with a fractional luminosity $f = 2.7 \times 10^{-5}$ (see Fig. 5). This fit also highlights where the spectrum departs from a blackbody. The most prominent discrepancy occurs at >160 μm, where the observed fluxes are higher than those of the blackbody model. While such discrepancies could indicate that the disc spectrum contains multiple temperature components, or indeed features associated with specific dust compositions, it is more likely that these longest wavelength fluxes are contaminated with what is assumed to be background emission, since they include all flux within 40 arcsec of the star (see Section 2.1.2); these contaminating sources are accounted for in the modelling of Section 3.3.

---

[5] http://scanpiops.ipac.caltech.edu:9000

One thing that is clear from the SED, however, is that there is no evidence for a hot ($\gg 68$ K) component suggesting that the inner regions are relatively empty. This is supported by the star-subtracted 70 μm image (Fig. 2). Although an inner hole is not evident as a decrease in surface brightness in the central pixels, the resolution is such that the central pixels are expected to include flux from the outer regions of the disc. However, the image would be expected to be much more centrally peaked if there was dust close to the star, and this point is quantified through modelling in Section 3.3.

3.3 Models

The aim of the modelling is to arrive at an axisymmetric circumstellar disc structure that fits all of the images in Fig. 1 as well as the spectrum in Fig. 5. Clearly this will not be possible at the longer wavelengths without also including background sources. Given the interpretation in previous sections, the simplest morphology for the background sources is that there are two point sources, one ∼27 arcsec to the west, and another ∼10 arcsec to the north. Thus, in the models all images include such sources at offsets from the star that are free parameters (but that are the same for all wavelengths), with fluxes at each wavelength that are also free. All of these parameters are determined by a best fit to the images, however, we concluded that the quality of the 500 μm observations was not sufficient to derive fluxes for the individual background sources at this wavelength. The models also include emission from the point-like star at the level derived for the photosphere (Section 3.1).

Different models are tried for the disc profile, discussed in more detail below. However, there are some common elements between all models, and how the models are assessed, that are described here. First, no attempt is made to constrain the grain properties or size distribution, since in the absence of spectral features this will be degenerate with other assumptions. Rather it is assumed that the emission spectrum of the disc at any given radius resembles a modified blackbody that is defined by its temperature, T, and the wavelength beyond which the spectrum is modified, λ_0, and the modification to the spectral slope β (i.e. the spectrum has an additional factor $\propto (\lambda_0/\lambda)^\beta$ for wavelengths $\lambda > \lambda_0$). The parameters λ_0 and β are left free, but given the level of confusion at submm wavelengths they are poorly constrained, as discussed further below. The temperature is assumed to be $T = f_T T_{bb}$, where $T_{bb} = 266r^{-1/2}$ is the temperature (in K) that blackbodies would attain at a distance r (in au) for this stellar luminosity, and f_T is a free parameter. It was not found to be necessary to change the $-1/2$ power-law radial dependence of temperature in the models. In models that include multiple components, the different components were sometimes allowed to have different properties (f_T, λ_0, β).

The emission from different annuli in the disc model was then determined by the vertical geometrical optical depth distribution $\tau(r)$, that had different assumptions in the different models. An image of the model was made by integrating the flux along the line-of-sight of different pixels given two free parameters that define the orientation of the orbital plane (the inclination to our line-of-sight, I, and the PA); if the pixels undersampled the disc structure a denser grid of pixels was used, and then rebinned, to ensure that all of the disc flux was captured. The background sources and the star were added to individual pixels, and the whole image convolved with an appropriately oriented telescope PSF (e.g. Kennedy et al. 2012).

To quantify the success of the model, the model images were subtracted from the observed images, then divided by the 1σ pixel-to-pixel uncertainty given in Fig. 1, following which the resulting image was squared. This was then used to derive a χ^2 by summing over pixels near the disc.[6] A χ^2 was also derived from the SED, but only including the wavelengths where the photometry was not derived from one of the *Herschel* images, i.e. including the *AKARI* 18 μm, MIPS 24 μm and the IRS spectrum (but not the MIPS 70 μm as previously noted).

The χ^2 for the different images and that from the SED were then summed using the following weighting. Each photometric data point from the literature received a relative weight of 1. Images were weighted by the area above the 3σ flux level divided by the area above the same flux level of the PSF scaled to the image peak. With this prescription, an unresolved image has the same weight as a photometric data point, and resolved images are weighted by the number of resolution elements that the source covers.

Since the location of the star in the images is not well constrained, this location is also left as a free parameter for the three observations (100/160, 70/160 and 250/350/500). The free parameters of the model are thus: six for the location of the star, four for the offsets of the two background sources, 12 for the fluxes of the background sources at the six wavelengths, two for the orientation of the disc plane, three for the dust properties (f_T, λ_0, β), plus those describing the spatial distribution.

With so many parameters, finding the best fit by grid methods is prohibitive. Instead, we initially find reasonably fitting models by varying parameters by hand, which are further refined with least-squares minimization. The minimization step means that our models at least lie at a local minimum in parameter space, but does not exclude the possibility of a better fit in a different region of parameter space. Nevertheless, since the models provide a reasonable fit to the observations, we believe that they are at least representative of the variety of models that can fit the data. However, we prefer not to trust the uncertainties in the model parameters returned by the minimization process, and quote these based on other considerations as outlined below.

3.3.1 Single extended component

The simplest model tried had a radial profile given by $\tau(r) = \tau_0(r/r_{min})^p$ between inner and outer radii r_{min} and r_{max}. The best fit found was for $r_{min} = 29$ au, $r_{max} = 350$ au, $p = -1.1$, $\tau_0 = 6.9 \times 10^{-5}$, $I = 77°$, $f_T = 1.9$, $\lambda_0 = 220$ μm and $\beta = 1$. The background sources were found to be offset by $(-27, +2$ arcsec$)$ and $(-4, +7$ arcsec$)$ with fluxes resembling cool emission with temperatures of <40 K (see Fig. 6), and so are consistent with extragalactic emission. The resulting model images are shown in Fig. 7, that can be compared directly with Fig. 1, since the figures employ the same colour scale and contours. Fig. 7 also shows the residual image (i.e. observed minus model). Clearly the model provides an excellent fit to the observations, and the residuals in the vicinity of the star are consistent with the noise elsewhere on the image; there is no evidence for any asymmetry in the disc structure. The resulting reduced χ^2 was 1.51.

Although the algorithm provides uncertainties on the model parameters, the most instructive way to qualify how well the radial distribution is constrained is to compare this result with an alternative model that provides a comparable fit to the image (Section 3.3.2).

---

[6] Near here means those pixels likely to contain non-zero flux. These were chosen by taking an observed image and setting all pixels over 3σ to 1, and setting those below 3σ to 0, then convolving with the PSF and retaining pixels >0.1. This procedure yields a mask that is somewhat larger than the disc, ensuring that models are also penalized for being too extended.
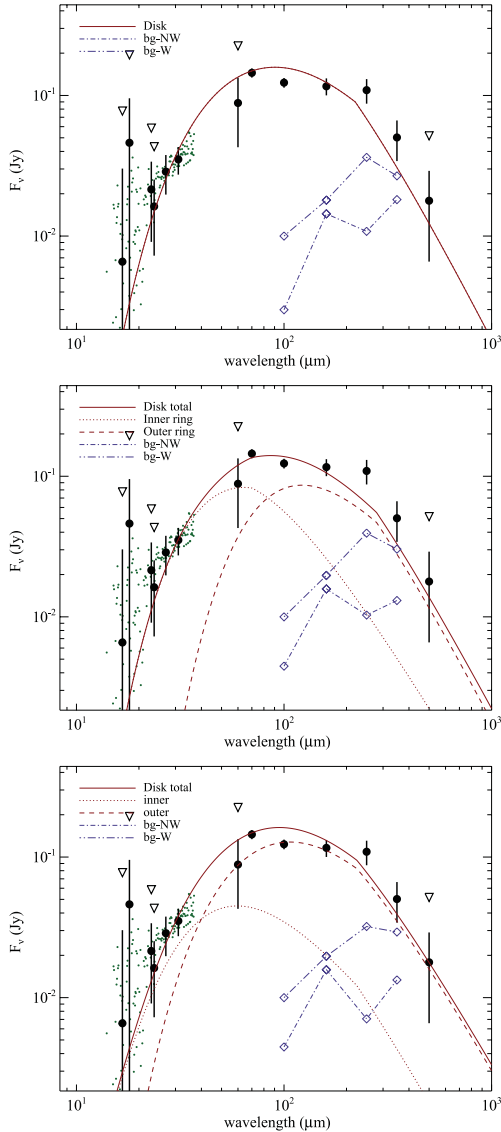
Figure 6. Model SEDs of 61 Vir. The top panel shows the continuous 29–350 au dust distribution model (Section 3.3.1), the middle panel shows the 40 and 90 au ring model (Section 3.3.2) and the bottom panel shows the collisionally evolved pre-stirred 1–350 au model (Section 3.3.3). Fluxes shown in black are those observed less that of the photosphere, i.e. these are the same fluxes plotted in grey on Fig. 5, except that here detections that are below 3σ are plotted both at their measured value (with their 1σ uncertainty) and as triangles to indicate the 3σ upper limit. The model disc fluxes are shown with a thick red line, and contributions of the two components of the bottom two models have also been separated out with dotted and dashed lines, for the innermost and outermost component, respectively. The inferred spectra of the background sources are shown in blue.

However, both models come to similar conclusions on the parameters defining the dust properties. These show that the factor by which the dust temperature exceeds that of black bodies in thermal equilibrium, f_T, is well constrained, since it is essentially set by the emission spectrum. This factor is in line with expectations that it should be greater than unity, because the $\sim1\,\mu m$ dust grains that dominate the cross-sectional area of a debris disc absorb starlight efficiently but reemit inefficiently at longer wavelengths (e.g. fig. 3 of Bonsor & Wyatt 2010). It is also in line with observa-

tions of other discs that have been imaged (e.g. fig. 9 of Rodriguez & Zuckerman 2012), since one would expect discs to be around f_T^2 times larger than would have been anticipated from their temperature assuming the grains to act like black bodies. On the other hand the factors λ_0 and β are poorly constrained, since they depend on the fraction of the emission seen in the 350 and 500 μm images that comes from the disc, and the resolution is insufficient to separate the disc emission from the background sources (particularly that to the north), which moreover may have a more complicated structure than the two-point source model that has been assumed; the circumstellar emission will be less confused in >5–10 yr once the star has moved away from the background sources (see Fig. 3, middle). The uncertainty on the disc inclination is estimated as $\pm4°$.

This model was also used to predict the corresponding scattered light images, under the assumption that the grains scatter light isotropically and have a constant albedo ω at all optical wavelengths at which they interact with starlight. These model images were then compared with the constraints on the optical surface brightness set by the STIS images in Section 2.2.3 to set constraints on ω. The scattered light in this model is brightest at its inner edge at around 3.7 arcsec, constraining the albedo to $\omega < 0.31$. This is not a definitive statement about the grain albedo, since other disc structures also fit the thermal emission and result in slightly different constraints on the albedos (see Sections 3.3.2 and 3.3.3). However, we note that $\omega < 0.31$ is consistent with the grain albedos inferred for other debris discs imaged in scattered light around solar-type stars (e.g. Backman et al. 2009; Krist et al. 2010; Golimowski et al. 2011), as well as for Solar system interplanetary dust particles (Kelsall et al. 1998).

3.3.2 Two radii

The next model had a radial profile given by two narrow rings at radii of r_1, r_2, each of which had a constant optical depth τ_1 and τ_2 across a width of 10 au, and with different particle properties f_{Ti}, λ_{0i}, β_i. The best fit found had $r_1 = 40\,au$, $r_2 = 90\,au$, $\tau_1 = 1.4 \times 10^{-4}$, $\tau_2 = 1.7 \times 10^{-4}$, with particle properties $f_{T1} = 1.9$, $\lambda_{01} = 70\,\mu m$, $\beta_1 = 0.53$, and $f_{T2} = 1.5$, $\lambda_{02} = 280\,\mu m$, $\beta_2 = 0.95$, with background sources with fluxes and locations very similar to those of Section 3.3.1 (see Fig. 6). Again the model provides an excellent fit to the observations (see Fig. 8), with residuals that look broadly similar to those of Fig. 7, and has a total reduced χ^2 of 1.94.

As this model provides a comparable fit to the same set of observations, it illustrates the uncertainty in the radial profile. For example, we should not take too seriously the conclusion of Section 3.3.1 that the radial profile extends out as far as 350 au, since the contribution from the outermost regions beyond 100 au is negligible, even if the fit of a single component model is improved by including emission in these outer regions. The larger outer extent is favoured because there is emission out to 20 arcsec to the north-east at 70–160 μm. Fig. 1 shows this is not equally matched to the south-west. Since the two ring model does not include emission at such large distances, this results in significant ($>4\sigma$) residual emission being present ~20 arcsec east-north-east of the star in Fig. 8.

The resolution of the images is also not such that we can tell if the distribution between 30 and 100 au is continuous or concentrated in narrower features. Similarly the inner edge is not well known, but to explore this we consider a third model in Section 3.3.3. We do not attribute any physical significance to the fact that the two rings are inferred to have different λ_0 and β, which arises to
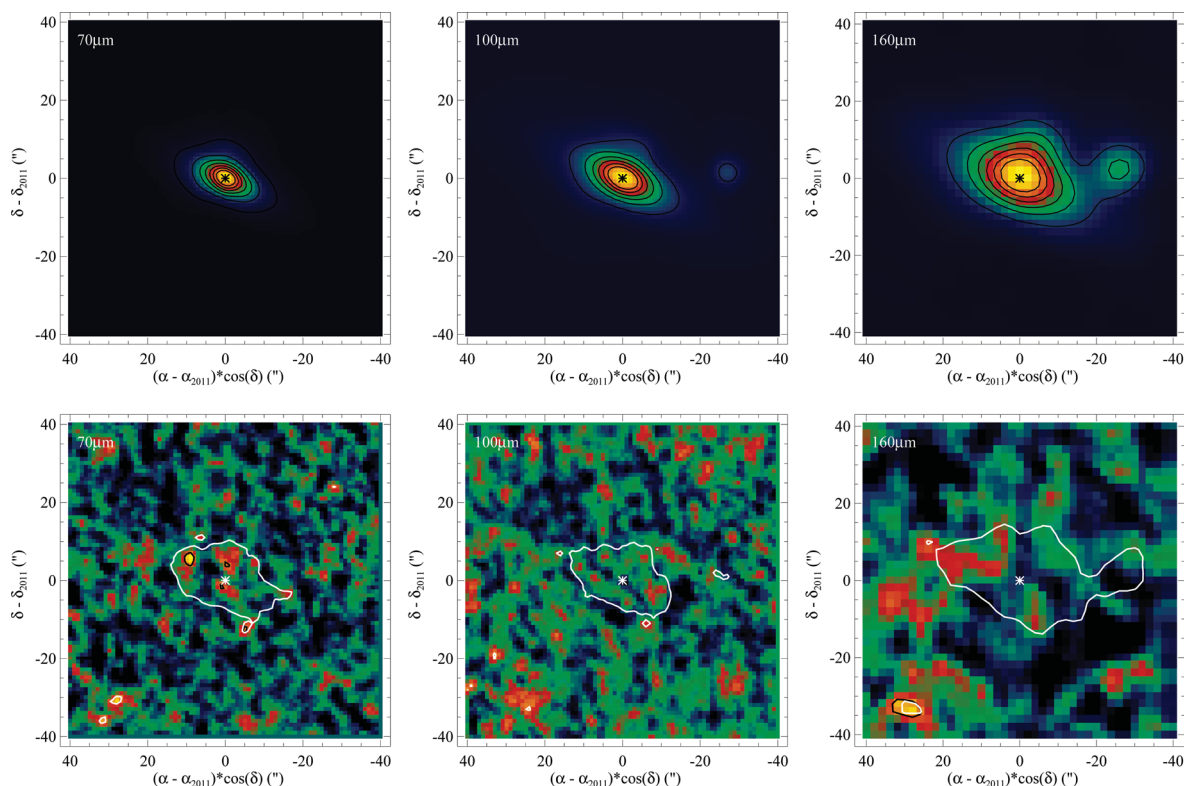
Figure 7. Model images of the PACS 70 μm (left), 100 μm (middle) and 160 μm (right) emission distribution towards 61 Vir using the single extended component model of Section 3.3.1 which has a continuous dust distribution from 29 to 350 au. The top row of images can be compared directly with Fig. 1, since these are model observations, and employ the same contours and colour scale. The bottom row are the residual images (observed minus model), with a colour scale that goes from -2 to $+6$ times the 1σ uncertainty in each observation, and contours are shown in black at $+4\sigma$. The white contour shows the region where the observed flux is above 4σ (from Fig. 1).

ensure an appropriate balance of flux from the two components at all wavelengths. Rather, again, we consider these parameters to be poorly constrained. With this model, the non-detection in the STIS images result in a constraint on the dust albedo of $\omega < 0.25$. This is slightly more stringent than the model of Section 3.3.1 as the emission in this model is more concentrated.

3.3.3 Collisionally evolved pre-stirred disc

This model is the same as that of Section 3.3.1, except that we also allow the optical depth distribution to extend continuously inward of r_{min} to an inner edge at r_0 with power-law index p_0 (which is positive so that optical depth increases with radius in this region). Thus, the disc surface density increases from an inner edge (at r_0) to a maximum (at r_{min}), then turns over and decreases towards the outer edge (at r_{max}).

Given that we have added parameters to a model that already had sufficient parameters to explain the observations, we do not intend to present a full exploration of this parameter space. Rather, the intention here is to test a hypothesis that the planetesimal disc initially extended all the way from an inner edge just outside the known planets at r_0 (at around 1 au) out to some large distance r_{max}, and that the inner regions of this disc (inside r_{min}) have since been depleted by collisional erosion, whereas the outer regions (beyond r_{min}) have yet to reach collisional equilibrium. If the disc is pre-stirred (see Wyatt 2008), in the sense that collisions between the planetesimals were destructive from shortly after the star reached the main sequence, then the inner regions would be expected to

attain an optical depth profile with $p_0 = 7/3$ (Wyatt 2008; Kennedy & Wyatt 2010; see Section 4.4). It is this model that we consider here. The physical interpretation of derived parameters such as r_{min} is discussed in Section 4.4, and a discussion of the *self-stirred* (Kennedy & Wyatt 2010; Kenyon & Bromley 2010) and *planet-stirred* (Mustill & Wyatt 2009) variants of this model is given in Section 4.5.

This model has a reduced χ^2 of 1.60, and as with the previous models we find an excellent fit to the data; e.g. Fig. 8 shows residuals that are very similar to those of the single extended component model of Fig. 7. The inner edge r_0 is not well constrained; it can extend all the way to the star because the surface density of the (collisionally depleted) inner region increases very steeply with radius so little emission originates from the innermost part of the disc. The model we present here has $r_0 = 1$ au at which radius the optical depth is $\tau_0 = 7.4 \times 10^{-9}$. The turnover occurs at $r_{min} = 43$ au, so has moved outwards compared to the inner edge of the single component model of Section 3.3.1 to account for the extra inner emission. The outer edge lies again at $r_{max} = 350$ au (but as noted above could be much closer). Other parameters are similar to the single component model, e.g. $\lambda_0 = 225$ μm, $\beta = 0.7, f_T = 1.8$, largely because the model assumed an optical depth profile in the inner regions that was steep enough to mean that this component is not a major contributor to the disc emission (Fig. 6).

Thus, the observations are consistent with a small level of emission being present within 30 au. To quantify this further, we repeated this modelling, but decreased p_0, keeping r_0 at 1 au, until the best fit with the assumed parameters was unacceptable. This procedure
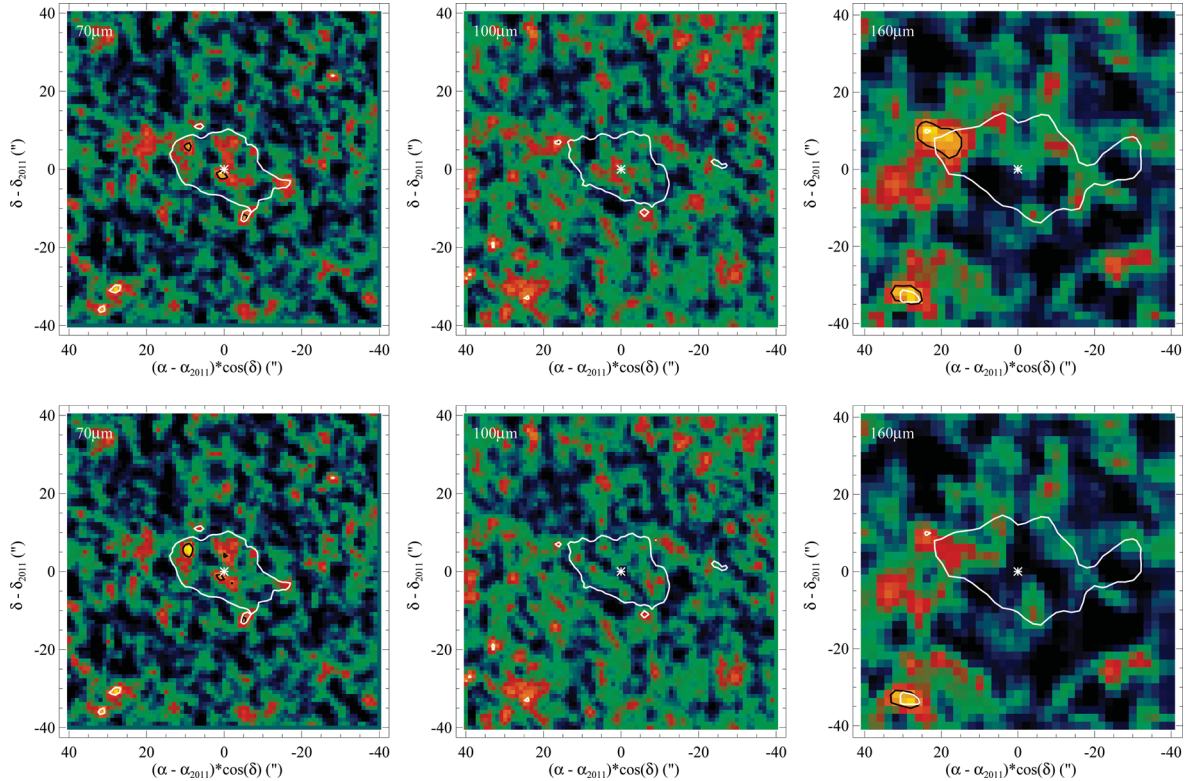
Figure 8. Residual images (observed minus model) of the PACS 70 μm (left), 100 μm (middle) and 160 μm (right) emission distribution towards 61 Vir. The top row shows the residuals of the best-fitting model of Section 3.3.2 which has two narrow rings at 40 and 90 au. The bottom row shows the residuals of best-fitting model of Section 3.3.3 which corresponds to a collisionally evolved pre-stirred disc that initially extended from 1 to 350 au. The colour scales and contours are the same as Fig. 7.

found that distributions with $p_0 \leq 1$ are ruled out, both because they result in a level of mid-IR emission that exceeds that seen in the IRS observations, and because the 70 μm image becomes too centrally peaked. In other words, the slope of the inner edge is not well constrained, except that we can say that it rises sharply enough for there to be negligible flux in the inner regions. From the IRS spectrum this means that the inner component must have a 10 μm flux below around 50 mJy (i.e. 2 per cent of the stellar photosphere) and a 32 μm flux below 54 mJy assuming the outer component does not contribute any flux at this wavelength (which is unlikely so the true flux limit will be lower). From the 70 μm image, the inner component must contribute below around 6 mJy (the 3σ point source uncertainty). The albedo constraint from the STIS non-detection is slightly higher than that of the previous models at $\omega < 0.57$, since the emission in this model is more diffuse.

4 IMPLICATIONS FOR THE 61 VIR PLANETARY SYSTEM

4.1 The 61 Vir planetary system

The data set of radial velocity measurements for 61 Vir has expanded since the observations reported in Vogt et al. (2010), allowing further consideration of the properties of its planetary system. Segransan et al. (in preparation) report 142 precise High Accuracy Radial velocity Planet Searcher (HARPS) radial velocities (averaged values per night) of 61 Vir between JD = 53037 and 55948 that confirm the existence of the inner two planets, with parameters consistent with the values of Vogt et al. (2010) (i.e. a 5.1 $M_{\oplus}$ planet at 0.05 au

and a 18.2 $M_{\oplus}$ planet at 0.218 au). However, the outermost planet (i.e. the 22.9 $M_{\oplus}$ planet at 0.478 au) has not been confirmed in the HARPS data at this point. The temporal variation of the log (R'_{HK}) activity index (which is also available from the HARPS spectra) shows that, although the star has been quiet most of the time, there was a burst of activity between JD = 54800 and 55220. Such active periods can influence the interpretation of longer periodicities in the data, and so affect our ability to extract longer period planets. As the existence of this planet is not crucial to the conclusions of this paper, this issue is not discussed further here.

Valuable constraints can also be set on the properties of planets that can be ruled out by the HARPS data (e.g. Mayor et al. 2011). Since the two-planet system fits the radial velocities to within $K \approx 1$ (in ms^{-1}), this crudely allows us to rule out planets on circular orbits at semimajor axes a_{pl} (in au) that are more massive than $M_{\mathrm{pl}} \sin i > 10K\sqrt{a_{\mathrm{pl}}}$ in $M_{\oplus}$. However the limit would be higher than this for planets on periods much longer than the length over which the observations have been taken (~8 yr). Fig. 9 shows the limit derived from an analysis of the HARPS data (excluding that obtained during the activity burst) from which the solution for the two inner planets has been subtracted. For each point in the mass–period diagram, a corresponding circular orbit is added to the residuals of the two-planet model, with 20 phase values (spaced equidistantly between 0 and 2π). For each phase, this process is repeated 1000 times with the residuals randomly permuted, and we consider that the planet is detected only if we see a signal in the resulting periodogram that is higher than the 1 per cent false alarm probability limit at all phases. The detection threshold obtained agrees well with that expected from the crude analysis above, and shows that the data
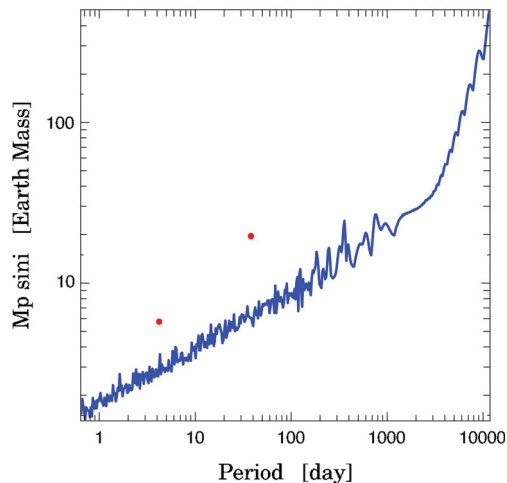
Figure 9. Detection limit derived from the HARPS radial velocities. The blue line indicates the limit above which planets on circular orbits would have been detectable in the data (see text for details). The red dots indicate the position of the two inner planets.

exclude planets that are more massive than Saturn with semimajor axes inside 6 au.

4.2 Interaction between known planets and debris

Since the planet masses given in Section 4.1 were derived from radial velocities the masses reported are actually $M_{pl} \sin i$ rather than M_{pl}, and the inclination of the planets' orbits to the sky plane (i) is unknown. Our observations determine the inclination of the disc's plane of symmetry to the sky plane to be 77°. If we assume that the planets' orbits are coplanar with the disc then their masses should be revised modestly upward by 3 per cent from the values given above. Such a small change would not affect previous conclusions in the literature about the dynamics of this system (Vogt et al. 2010; Greenberg & van Laerhoven 2012).

   However, the planets do not have to be coplanar with the disc, since the two are sufficiently spatially separated that there is little dynamical interaction between them. For example, although the planets' secular perturbations will make the orbits of disc particles precess so that their distribution would end up symmetrical about the invariable plane of the planetary system, the time-scale for this to happen is at least the secular precession time-scale. At 30 au this is 60 Gyr considering perturbations from the three Vogt et al. (2010) planets, and even longer if the outermost planet is excluded. This also precludes the disc having been stirred by these planets (Mustill & Wyatt 2009), i.e. the collisional cascade in the disc must have been ignited by some other mechanism (see Section 4.5). Rather, if there is to be an interaction between the known planets and the disc there would need to be planets in the intervening 1–30 au region, either to allow disc material to be scattered to these inner regions (e.g. Bonsor & Wyatt 2012), with implications for the habitability of the inner planets (e.g. Horner & Jones 2010), or for the planets' gravitational perturbations to influence the intervening planets which in turn influence the outer regions (e.g. Zakamska & Tremaine 2004).

   The assumption that the planets and the debris disc are coplanar is justified by the premise that the debris disc and planets were born from the same protoplanetary disc, which had a single plane of symmetry. Nevertheless this does not guarantee that the two should remain coplanar, since the debris disc may have been perturbed by passing stars, and the planets could have undergone a dynamical interaction that misaligned their orbital planes (Naoz et al. 2011). The spin axis of the star can also become misaligned with the protoplanetary disc under certain conditions (Lai, Foucart & Lin 2011). In this respect it is worth noting that the stellar rotation period of 29 d and $v \sin i$ of $1.6 \pm 0.5\,\mathrm{km\,s^{-1}}$ suggest the stellar pole is inclined 72° to our line-of-sight, i.e. consistent with being nearly perpendicular to the debris disc's symmetry plane. Thus there is no evidence at the moment to suggest that the angular momentum vectors of the star, planets and debris disc are misaligned.

4.3 Intervening planets?

Given that an axisymmetric disc model provides a good fit to the observations (Section 3), disc asymmetries cannot be invoked as evidence for more distant planets as has been the case for other imaged discs (e.g. Wyatt 2008; Krivov 2010). However, the emptiness of the inner region does require an absence of planetesimals, and this emptiness can be readily explained if there are additional planets in the 1–30 au region, since such planets could dynamically deplete the region (e.g. Lecar et al. 2001). In Section 4.1 we already used the radial velocity data to set constraints on the planets that are allowed to exist within 6 au (and have remained undetected, see Fig. 9). It is not possible to set hard constraints on more distant planets, except for generalities such as that the planets cannot reside too close to the inner edge of the disc (Quillen 2006; Mustill & Wyatt 2012). However, in Section 4.4 we consider the possibility that no planets exist in the 1–30 au region.

4.4 Plausibility of pre-stirred extended disc model

In Section 3.3.3 it was suggested that the observed depletion could arise from collisional erosion, i.e. without requiring any planets to exist in the 1–30 au region. To confirm that this is a plausible explanation, we show here that the observationally inferred parameters for this model (r_{min}, τ_0 and p) correspond to physically plausible parameters within the context of this scenario.

   First we consider the regions beyond r_{min} which, in this interpretation, have yet to deplete, so can be used to determine the initial mass distribution of the debris disc; we will assume this initially extended all the way in to r_0 according to $\Sigma = \Sigma_0 (r/r_0)^p$, where Σ is the mass surface density (e.g. in $\mathrm{M_\oplus\,au^{-2}}$). The mass surface density simply scales with the optical depth according to the size distribution, which we assume to be a single power law with the -3.5 exponent expected (under certain ideal assumptions) for collisional equilibrium, from a maximum planetesimal size D_{max} (in km), down to the size at which dust is removed by radiation pressure. Using equation (15) of Wyatt (2008), for a $0.88\,\mathrm{M_\odot}$, $0.84\,\mathrm{L_\odot}$ star, assuming a solid density of $2700\,\mathrm{kg\,m^{-3}}$,

$$\Sigma/\tau = 0.19 D_{max}^{1/2} \tag{1}$$

(in $\mathrm{M_\oplus\,au^{-2}}$).

   For reference in later paragraphs, once we have estimated D_{max}, we will compare the mass surface density derived with that of a fiducial *minimum mass solar nebula* (MMSN), which contains $1.1\,\mathrm{M_\oplus\,au^{-2}}$ of solid material at 1 au, with surface densities falling off to larger distance as $(r/r_0)^{-3/2}$ (e.g. Weidenschilling 1977). The best-fitting model of Section 3.3.3 has an optical depth at 43 au of 4.8×10^{-5} which is around an order of magnitude higher than that in the Kuiper belt (see fig. 13 of Vitense, Krivov & Löhne

2010), and corresponds to a mass surface density at that location of $2.3 \times 10^{-3} D_{max}^{1/2}$ times that in the MMSN.

The plausibility of this interpretation comes down to whether it is reasonable to expect the transition to collisional equilibrium to occur at 43 au given the stellar age of 4.6 ± 0.9 Gyr. As well as the aforementioned parameters, the collisional lifetime of the largest planetesimals in the disc depends on their strength $Q_D^\star$ and eccentricity e (which sets collision velocities). For the assumptions above, this collisional lifetime can be estimated (see equation 13 of Wyatt et al. 2007a) to be

$$t_c(D_{max}) = 1.4 \times 10^{-3} r^{7/3} \left[Q_D^{\star 5/6} D_{max}^{1/2} e^{-5/3} \right] \tau^{-1} \qquad (2)$$

(in yr). In the inner regions that are assumed to be in collisional equilibrium this lifetime should be the age of the star, explaining why we set $p_0 = 7/3$ in Section 3.3.3.

Thus, for the collisional lifetime at 43 au to be equal to the 4.6 Gyr age of the star, the quantity in square brackets in equation (2) must be of order 2.4×10^4 (± 50 per cent due to the uncertainties in stellar age and disc optical depth and turnover radius). This quantity has been estimated from the detection statistics as a function of age for the ensemble of debris discs around A stars to be 7.4×10^4, with a dispersion of 1 dex about this average disc value (Wyatt et al. 2007b). For Sun-like stars the same process gives this quantity as 2.9×10^6 with a similar dispersion (Kains, Wyatt & Greaves 2011). So it appears that, for this interpretation to be valid, the properties of planetesimals around 61 Vir would have to be broadly similar to those of average A star debris discs, but would be in the 2σ minority when compared with debris discs known around Sun-like stars. The sense of this difference is that the planetesimals would have to be smaller, or on more elliptical orbits. We find that the required quantity is obtained for $D_{max} = 2$–5 km for $e = 0.05$–0.1 for two different strength laws, i.e. that of weak aggregates (Stewart & Leinhardt 2009) and that for low-temperature ice (e.g. Vitense et al. 2010).

To conclude on the pre-stirred model, we find that the observations can be explained if the disc is made up of planetesimals up to a few km in size, with a mass surface density around 0.4 per cent that of the MMSN. Despite its low mass, which is comparable with that of the Kuiper belt, the disc in this model is detectable because the mass is locked up in relatively small planetesimals. Such a low mass is somewhat at odds with the presence of planets, since if these have even modest rocky cores, then the solid mass surface density in the inner regions is at least an order of magnitude above the MMSN. Even if all of the mass inside 43 au in the hypothetical initial debris disc was placed in the planet region, that would only correspond to $0.2\,M_\oplus$. One would therefore have to conclude that the disc was initially much more massive, and that the majority of the mass has been depleted somehow, such as by inwards migration due to gas drag (or simply never having grown into planetesimals).

Remember though, that this conclusion is based on the premise that the 43 au peak arises from collisional evolution. If the inner edge is truncated by some other mechanism, then the debris disc could include much larger planetesimals and so be much more massive. For example, if the planetesimals were up to 2000 km in diameter the debris disc's mass surface density would be inferred to be around 10 per cent of a MMSN at 43 au. Given the uncertainties, this initial mass is more compatible with the known planets, but would still require the original protoplanetary disc to be significantly more massive than the remnant debris disc, and likely also that the planets we know today include a reasonable fraction of the mass that was originally inside 43 au.

4.5 Disc stirring mechanism

In the model discussed in Section 4.4, the disc was assumed to be stirred from early on, since that allowed us to equate the collisional lifetime (equation 2) with the stellar age. Such a model is called *pre-stirred* in Wyatt (2008), and makes no assumptions about the stirring mechanism.

A variant on the pre-stirred model, that includes a self-consistent consideration of the stirring mechanism, is the *self-stirred* model. In this model collisions in an extended planetesimal belt initially occur at low enough velocity for planetesimal growth to occur (Kennedy & Wyatt 2010; Kenyon & Bromley 2010). Such models allow planet formation processes to continue throughout the several Gyr lifetime of the star. Within such a model a peak in surface brightness naturally corresponds to the location at which planetesimals have recently grown to around Pluto size, since at this time gravitational scattering stirs neighbouring planetesimals resulting in enhanced dust production. For the growth of Pluto-size objects, i.e. those large enough to stir the disc, to have reached 43 au after 4.6 Gyr of evolution, this would require the original protoplanetary disc of 61 Vir to be less than 0.01 per cent of a MMSN (see equation 9 of Kennedy & Wyatt 2010). Since this would require the disc to be made up of entirely of subkm-sized planetesimals, which is contrary to the premise of the model that planetesimals are growing up to Pluto size, we do not consider this to be a viable explanation.

Fully formed planets that are well separated from the disc can also stir the disc through their secular perturbations, i.e. the *planet-stirred* model (Mustill & Wyatt 2009). We already showed in Section 4.1 that the known planets cannot have stirred the disc given the age of the star. However, planetary perturbations are a plausible stirring mechanism if there are planets in the 1–30 au region, since the proximity of such planets to the disc means that their perturbations could affect the disc within the stellar age. For example, for a planet with an eccentricity of 0.1 to have stirred the disc at 30 au within 4.6 Gyr requires its mass to be $>150 a_{pl}^{-3}$ (in $M_\oplus$), where a_{pl} is its semimajor axis in au (see equation 15 of Mustill & Wyatt 2009). Such planets are not ruled out by the current radial velocity observations (see Fig. 9).

4.6 Summary

To conclude, we know that there are planets within 1 au, and that there are planetesimals producing dust beyond 30 au, but the only thing we can say for certain about the 1–30 au region is that there is a relative dearth of planetesimals within 30 au compared with the more distant regions. The presence of planets in the 1–30 au region would naturally explain the absence of planetesimals, but the emptiness of this region could also be explained by collisional erosion, i.e. it could have been full of km-sized planetesimals that were subsequently depleted through mutual collisions that turned them into dust that was then removed by radiation forces. The latter explanation must also invoke a mechanism that stirs the disc (so that collisions are erosive). This would be readily explained if there were planets in the 1–30 au region, but could be inherent in the debris disc formation process.

5 LOW-MASS PLANETS AND DEBRIS: IS THERE A CORRELATION?

The coexistence of planets and debris around the eighth nearest G star prompted us to reconsider the lack of correlation between the two populations. In particular, we considered if earlier studies found

no correlation (e.g. Greaves et al. 2004; Moro-Martín et al. 2007; Bryden et al. 2009) because at that time radial velocity studies were only sensitive to relatively massive planets. Here we suggest that a correlation does indeed exist for low-mass planets.

5.1 Nearest 60 G star sample

To assess the existence of a correlation with low-mass planets we considered a restricted but unbiased sample comprised of the nearest 60 G stars (see Phillips et al. 2010). The sample size was restricted to allow a thorough analysis of individual stars; an analysis of a larger sample is deferred to Moro-Martín et al. (in preparation).

Out of this sample, 11 are reported in the literature to have planets, all of which were found in radial velocity surveys. We further subdivided this sample into those that have at least one massive planet, which we defined as a system with a planet more massive than $>95\,M_\oplus$ (i.e. Saturn mass) (hereafter called the high-mass planet sample), and those with only low-mass planets (hereafter called the low-mass planet sample). The high-mass planet sample comprises five systems (HD 146513, 47 UMa, μ Ara, 51 Peg, HD 190360) and the low-mass planet sample six systems (HD 20794, 61 Vir, HD 102365, HD 69830, HD 136352, HD 38858) that are described further in Table 2.

It may be questioned whether this division is appropriate, given that longer observations may reveal systems currently classified as having only low-mass planets to have more massive planets at larger distances. However, the radial velocities for 61 Vir show that there can be no planets more massive than Saturn orbiting within 6 au in this system (Section 4.1). So if more massive planets do exist they would have to be at larger separation, and the system would not have been classified as a high-mass planet system in this study. In other words, our classification of a low-mass planet system requires that there are planets detected above the blue line on Fig. 9, but that none of these is more massive than Saturn (or this would have been classified as a high-mass planet system), noting that the exact threshold will vary slightly between stars.

Of the high-mass planet sample, all have been observed with *Spitzer* at 70 μm, and all but HD 190360 were also observed with *Spitzer* at 24 μm (although fairly stringent limits do exist for this

source from *IRAS* 25 μm observations). None was found to have excess emission from circumstellar debris (Bryden et al. 2009). A detection rate of 0/5 is consistent with the number of detections that would be expected if the presence of debris is uncorrelated with the presence of planets, since nearby stars have a 14–16 per cent detection rate with *Spitzer* (Trilling et al. 2008; Bryden et al. 2009).

Note that if the Sun had been included in this sample Jupiter would fall above the detection threshold of radial velocity surveys, and so the Sun would have been classified as a high-mass planet system. Although we know the Sun has a debris disc, this is much lower in brightness compared with the discs known around nearby G stars (e.g. Greaves & Wyatt 2010), and its thermal emission would not have been detectable in any current debris disc survey. This illustrates that the lack of debris disc detections around high-mass planet systems does not necessarily mean that these stars are completely clear of debris, since they could have discs below the detection threshold. Just as it was important to quantify what we mean by a system with high- and low-mass planets (see above, and Fig. 9), so it is important to also quantify what we mean by a system without debris; this is discussed further in Section 5.2.6.

5.2 Debris around the low-mass planet sample

In contrast to the high-mass planet sample, 4/6 of the low-mass planet sample are found to have debris. The debris towards three of these (61 Vir, HD 69830, HD 38858) was already known about from *Spitzer* (Beichman et al. 2006; Bryden et al. 2006). This is already a high detection fraction, because Poisson statistics show that the detection of ≥ 3 in a sample of six when the expected detection rate is 15 per cent is a 6.5 per cent probability event. This was not noted previously, because the planetary systems were only discovered since the *Spitzer* debris detections were reported. Excess emission towards HD 20794 was not reported from early analysis of the *Spitzer* observations (Beichman et al. 2006), but was detected by *Herschel* as part of the DEBRIS program, and this discovery is reported here for the first time. Below we provide more details on the debris towards members of the low-mass planet sample.

Table 2. Nearest 60 G stars with planets.

Star name	Planets (a, M_{pl})	Debris (r, f)	References
High-mass planet systems			
HD 147513	(1.32 au, 400 $M_\oplus$)	None detected	1, 11
47 UMa	(2.1 au, 840 $M_\oplus$), (3.6 au, 180 $M_\oplus$), (11.8 au, 550 $M_\oplus$)	None detected	2, 11
μ Ara	(0.09 au, 11 $M_\oplus$), (0.92 au, 170 $M_\oplus$), (1.5 au, 560 $M_\oplus$), (5.2 au, 600 $M_\oplus$)	None detected	3, 11
51 Peg	(0.05 au, 160 $M_\oplus$)	None detected	4, 11
HD 190360	(0.13 au, 18 $M_\oplus$), (3.9 au, 500 $M_\oplus$)	None detected	5, 11
Low-mass planet systems			
HD 20794	(0.12 au, 2.8 $M_\oplus$), (0.20 au, 2.5 $M_\oplus$), (0.35 au, 5.0 $M_\oplus$)	(19 au, 4×10^{-6})	6, 12, 13
61 Vir	(0.05 au, 5.3 $M_\oplus$), (0.22 au, 19 $M_\oplus$), (0.48 au, 24 $M_\oplus$)	(29–350 au, 3×10^{-5})	7, 13
HD 102365	(0.46 au, 17 $M_\oplus$)	None detected^a	8, 12, 13
HD 69830	(0.08 au, 11 $M_\oplus$), (0.19 au, 13 $M_\oplus$), (0.63 au, 19 $M_\oplus$)	(1 au, 2×10^{-4})	9, 14
HD 136352	(0.09 au, 5.5 $M_\oplus$), (0.17 au, 12 $M_\oplus$), (0.41 au, 10 $M_\oplus$)	None detected^a	10, 12
HD 38858	(1.0 au, 32 $M_\oplus$)	(102 au, 8×10^{-5})	10, 12, 15

^{a}See Fig. 11 for constraints on disc luminosity.
Notes. References: 1 – Mayor et al. (2004); 2 – Gregory & Fischer (2010); 3 – Santos et al. (2004); 4 – Mayor & Queloz (1995); 5 – Vogt et al. (2005); 6 – Pepe et al. (2011); 7 – Vogt et al. (2010); 8 – Tinney et al. (2011); 9 – Lovis et al. (2006); 10 – Mayor et al. (2011); 11 – Bryden et al. (2009); 12 – Beichman et al. (2006); 13 – This work; 14 – Beichman et al. (2011); 15 – Lawler et al. (2009).
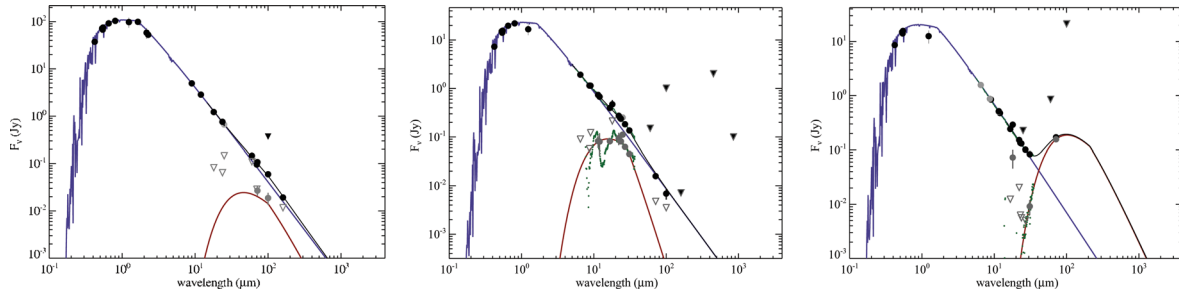
Figure 10. SEDs for low-mass planet systems with debris. Left: HD 20794; middle: HD 69830; right: HD 38858. Total fluxes are black points, open circles are predicted photospheric fluxes and grey points are photosphere subtracted fluxes. The photospheric model is shown with a blue line, and is a fit to data at wavelengths short enough that no excess is present. Longer wavelength fluxes are fitted as a modified blackbody at the temperatures given in the text which is shown with a red line. The total flux from the models (photosphere+disc) is shown with a black solid line.

5.2.1 HD 20794

At 6.0 pc the G8V star HD 20794 is the fifth nearest G star to the Sun; its age deduced from chromospheric Ca II H&K is 6.2 Gyr with 50 per cent uncertainty (Vican 2012). A non-detection with *Spitzer* was reported in Beichman et al. (2006), but a reanalysis of *Spitzer* data, and a remodelling of the stellar photosphere, shows that at 70 μm the observed flux of 106.7 ± 5.8 mJy is in fact significantly higher than the photospheric level of 80.9 mJy. The PACS observations also show a marginal excess at 70 μm of 97 ± 5.5 mJy (the photosphere is 84.2 mJy in this bandpass), and a significant excess at 100 μm of 59.0 ± 4.8 mJy (compared with just 41.0 mJy of photospheric flux), both measured with a 15 arcsec aperture. Although only marginal levels of excess were measured with MIPS at 24 μm (758.8 ± 7.6 mJy compared with a 741.5 mJy photosphere) and with PACS at 160 μm (20.6 ± 2.8 mJy from a PSF fit to the image, compared with a 15.8 mJy photosphere), these observations provide additional constraints that help pin down the temperature of the excess to 110 ± 35 K with a fractional luminosity of 4.3×10^{-6} (see Fig. 10).[7] The stellar luminosity of $0.66\,L_\odot$ puts the dust at 5.2 au if it emits like a blackbody, but we estimate its location using the same $f_T = 1.9$ factor derived for 61 Vir to predict its location to be around 19 au, noting that the uncertainty in the temperature, as well as that inherent in converting this to a radial location, means this location cannot be considered well constrained until the disc has been resolved.[8]

5.2.2 HD 102365

At 9.2 pc the G2V star HD 102365 is the 12th nearest G star to the Sun; its age deduced from chromospheric Ca II H&K is 5.7 Gyr (Vican 2012). The previous non-detection with *Spitzer* (Beichman et al. 2006) is confirmed in our reanalysis of the data at 70 μm (47.5 ± 4.5 mJy observed for 40.1 mJy photosphere) and 24 μm (363.1 ± 3.6 mJy observed for 366.9 photosphere). This is further strengthened by a non-detection of excess in PACS images at both 100 μm (15.9 ± 2.0 mJy observed for 20.3 mJy photosphere) and 160 μm (3.0 ± 4.4 mJy observed for 7.8 mJy photosphere), where both measurements were made by fitting template PSFs to

the images. This star has a binary companion at 23 arcsec projected separation, corresponding to an expected semimajor axis of 297 au (Allen, Poveda & Herrera 2000). We fit the photometry available for the companion to estimate an effective temperature of 2699 K and note that its 0.7 mJy photosphere is not detected in the 100 μm maps (-1.7 ± 2.0 mJy was measured at the binary location).

5.2.3 HD 69830

At 12.6 pc the G8V star HD 69830 is the 22nd nearest G star to the Sun; its age deduced from chromospheric Ca II H&K is 5.7 Gyr (Vican 2012). The excess towards this star has been analysed in great detail, since its IR spectrum contains numerous spectral features that provide valuable information on the composition of the dust. The reader is referred to Beichman et al. (2011) for more details of the observations, and here we summarize that the dust temperature puts it at ∼1 au, a location consistent with high-resolution mid-IR imaging and interferometry (Smith, Wyatt & Haniff 2009), and that its composition is similar to that of main-belt C-type asteroids in the Solar system. This location is at odds with the age of the star, since steady state collisional erosion of a planetesimal belt at 1 au should have reduced the mass of such a belt to levels far below that observed (Wyatt et al. 2007a). This leads to the conclusion that the dust must be either transient (e.g. the product of a recent collision), or that it is replenished from a more distant planetesimal belt where longer collisional time-scales mean that significant mass can survive (Wyatt et al. 2007a; Heng 2011). Far-IR observations have so far failed to find evidence for any outer belt (Beichman et al. 2011).

5.2.4 HD 136352

The G2V star HD 136352 is 14.8 pc from the Sun; its age deduced from chromospheric Ca II H&K is 6.4 Gyr (Vican, personal communication). No excess was reported towards this star with *Spitzer* at 70 μm (17.5 ± 5.1 mJy observed for 19.9 mJy photosphere; Beichman et al. 2006). This star was not observed by *Herschel* as part of the DEBRIS survey because of the high background level (Phillips et al. 2010).

5.2.5 HD 38858

The G2V star HD 38858 is 15.2 pc from the Sun; its age deduced from chromospheric Ca II H&K is 6.2 Gyr (Vican, personal communication). Excess at 70 μm was detected with *Spitzer* (153.7 ± 9.8 mJy observed for 15.0 mJy photosphere; Beichman et al. 2006),

---

[7] Note that the marginal excesses are plotted as upper limits on Fig. 10, but explain why the model fit for the excess flux on that figure goes slightly under the two significant detections.

[8] The 70 and 100 μm PACS observations show tentative evidence for extension at around the predicted scale, which is why fluxes were derived using an aperture at these wavelengths.

and later excess in the mid-IR spectrum was measured allowing the temperature to be determined and a dust location estimated at 12–29 au (Lawler et al. 2009). Like HD 136352, this star was not observed by *Herschel* as part of the DEBRIS survey because of the high background level (Phillips et al. 2010). For consistency with our interpretation of other sources, we repeat the analysis of its excess spectrum (see Fig. 10), and use the inferred dust temperature of 50 K to estimate a location from this 0.83 $L_{\odot}$ star as 102 au (again using the $f_T = 1.9$ factor inferred for 61 Vir). This size is consistent with the marginal extension of the MIPS 70 μm emission that can be fitted by a ring of size around 100 au size (section 5.2.3 of Lawler et al. 2009).

5.2.6 Summary

The detection rate of 4/6 is much higher than that seen in the background population. Although the analysis included observations with *Herschel*, in fact all of the detections were present in the *Spitzer* data, and so it may be reasonable to compare this detection rate with the 15 per cent of Sun-like stars found to have excess by *Spitzer*. Poisson statistics shows that detecting ≥4 from a sample of six for an expected detection rate of 15 per cent is a 1.4 per cent probability event. If instead the 4/6 rate was compared with the detection rate of discs found by *Herschel* in an unbiased population of Sun-like stars,[9] which is around 20–25 per cent, a rate this high would have been up to a 6 per cent probability event (for a 25 per cent detection rate). Thus, although this analysis is necessarily subject to small number statistics, it appears to be very unlikely that the low-mass planet sample has as low a detection fraction as other Sun-like stars. As one of the two low-mass planet systems without detected debris is a wide binary system, the high disc fraction would be further enhanced if the sample was restricted to single low-mass planet systems, though having a wide binary companion does not necessarily preclude the presence of debris (Trilling et al. 2007; Rodriguez & Zuckerman 2012).

Note that we are only claiming that the debris incidence rate is higher around stars with low-mass planets (that are detectable in current radial velocity surveys), not that all low-mass planet systems have detectable debris. Indeed this appears unlikely given that low-mass planetary systems may be present around 30–50 per cent of stars (Mayor et al. 2011), and that only 15 per cent of stars have debris that was detectable with *Spitzer*. Also we cannot comment on any correlation with planets closer to Earth mass that would be below the detection threshold of radial velocity surveys (e.g. Fig. 9), though such planets may be common (e.g. Melis et al. 2010; Borucki et al. 2011).

Likewise it is important to clarify that a detectable debris disc in this context implies that the fractional luminosity and disc temperature lie above the appropriate lines on Fig. 11. Although the detection thresholds are similar for the different stars in the low-mass planet sample, there is a dispersion in sensitivity to large cold discs (<100 K), and it should be acknowledged that a disc with the same fractional luminosity and temperature as that of HD 20794 would not have been detectable around all of the sample. Nevertheless, the same would be true of discs that could have been detected around the rest of the nearest 60 G star sample.
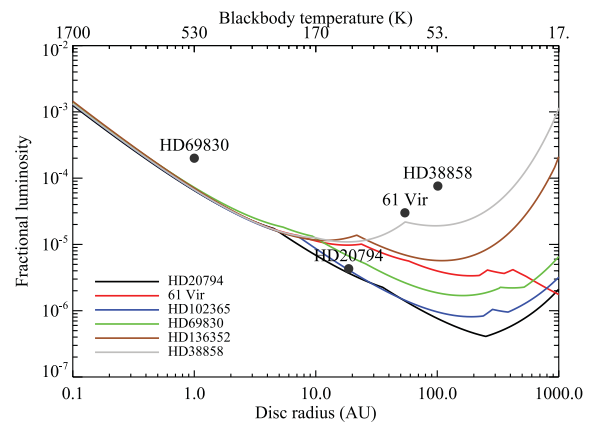
Figure 11. Parameter space for which excess emission from a debris disc would have been discovered in existing observations of the stars in the low-mass planet sample. The limits are derived by assuming that the star has a disc with a given fractional luminosity ($L_{ir}/L_{\star}$) and temperature (which is translated into disc radius using $f_T = 1.9$), and determining whether that emission would have been detectable in the observations at any wavelength at which the star was observed using equations (8) and (11) of Wyatt (2008) with the modification of Lestrade et al. (2009) for discs extended beyond the beam. The limits at different disc temperatures are dominated by different wavelengths (e.g. temperatures above 170 K are limited by MIPS 24 μm observations, with longer wavelengths constraining lower temperatures). The limits for different stars in the sample are plotted with different colours, and the black dots denote the parameters derived for the discs detected around four of the sample.

We defer a detailed consideration of the planet correlation to a later paper (Moro-Martín et al., in preparation), but note that the discovery of a debris disc around an M star with low-mass planets could suggest that this trend also continues to lower mass stars (Lestrade et al., in preparation).

5.3 Implications for planet formation

The correlation summarized in Section 5.2.6 suggests that, even if not directly connected, the formation of a system that was conducive to the formation of low-mass planets was also conducive to large quantities of planetesimals remaining in the system after several Gyr of evolution. This may be connected to a different correlation, in which stars with high-mass planets tend to be metal rich whereas those with low-mass planets have no bias in metallicity (Sousa et al. 2011), and neither do stars that host debris discs (Greaves, Fischer & Wyatt 2006; Maldonado et al. 2012).

Ideally the debris discs in low-mass planetary systems would share some characteristics that could both point to a reason for the correlation between these phenomena, and help identify systems as having low-mass planets through study of their debris discs. However, Table 2 shows that debris discs in low-mass planetary systems have a range of radii (1–350 au) that spans the range of known debris discs. Thus, planetesimals in low-mass planetary systems could either be at large distances from the planets (like 61 Vir, HD 20794 and HD 38858), or some of those planetesimals could be in close proximity to the planets, at least at some point in their evolution (like HD 69830).

Why might such a correlation exist? Here we consider the two scenarios that have been proposed for the formation of low-mass planet systems: (i) that the planets formed further out but then migrated in, perhaps gaining mass as they migrate (Alibert et al.

2006; Terquem & Papaloizou 2007; Ida & Lin 2010), or (ii) that they formed in situ in which case significant solid mass (50–100 $M_\oplus$) would have to be concentrated within 1 au (Hansen & Murray 2012).

Although not without issues in comparison with exoplanet statistics (McNeil & Nelson 2010), formation scenario (i) seems to be perfectly suited to leaving large quantities of outer debris. Payne et al. (2009) showed that the migration of the planets through a planetesimal disc is an inefficient process, in the sense that not all of the planetesimals are accreted or ejected by the migrating planets. Rather, many planetesimals are left stranded in the region through which the planets recently migrated. As long as there were no more distant planets that subsequently migrated in thus depleting this region, these planetesimals could be dynamically stable over long time-scales, but would predominantly deplete through mutual collisions.

Formation scenario (i) could also be applied to the formation of close-in massive planets. However, in this case the stronger gravitational perturbations of the migrating planets would result in the ejection or accretion of a larger fraction of planetesimals (though not necessarily all of them, e.g. Raymond, Mandell & Sigurdsson 2006). Moreover the migration of multiple high-mass planets may result in a dynamically unstable configuration, unless this can be prevented by resonance locking, in which case the ensuing instability could deplete any remaining planetesimals (e.g. Gomes et al. 2005; Raymond et al. 2011).

Formation scenario (ii) may also be conducive to forming an outer planetesimal belt, depending on how efficiently the solid mass is accreted on to planets. If even a small fraction of the planetesimal mass is scattered on to highly eccentric orbits, it would form a miniscattered disc of planetesimals with pericentres in the vicinity of the planets but apocentres extending out to large distances. If this happened during the protoplanetary disc phase, interaction with solid or gaseous material in the outer planetary system could then pull the pericentres of scattered planetesimals away from the planets (i.e. through gas drag or dynamical friction). This could prevent the planetesimals from being ejected and leave them in a long-lived extended disc configuration.

Again, application of scenario (ii) to the formation of massive planets would be less favourable to the formation of massive outer debris discs. This is because planetesimals are more readily ejected by more massive planets (e.g. Tremaine 1993), on time-scales that would be shorter compared with the time-scale for the outer disc to decouple the planetesimals from the planets' gravitational influence.

It thus seems plausible that high levels of outer debris could be a natural outcome of systems that form only low-mass planets.

6 CONCLUSIONS

Observations from the DEBRIS key programme are presented that resolve the structure of the debris disc around the exoplanet host star 61 Vir (Section 2). Modelling shows that the dust extends from 30 au out to at least 100 au in a nearly edge-on configuration (Section 3). There is likely little interaction between the disc and the known planets, which are at <0.5 au. The lack of planetesimals in the <30 au region could be explained by the existence of planets in this region, but the depletion can also be explained by collisional erosion (Section 4). Considering a sample of the nearest 60 G stars there is an emerging trend that stars which, like 61 Vir, only have low-mass planets are more likely to have detectable debris (Section 5). We attribute this trend to the fact that the formation processes that make low-mass planets are likely to also result in large quantities of distant debris.

REFERENCES

Alibert Y. et al., 2006, A&A, 455, L25
Allen C., Poveda A., Herrera M. A., 2000, A&A, 356, 529
Backman D. et al., 2009, ApJ, 690, 1522
Batygin K., Laughlin G., 2011, ApJ, 730, 95
Beichman C. A. et al., 2006, ApJ, 652, 1674
Beichman C. A. et al., 2011, ApJ, 743, 85
Bonsor A., Wyatt M. C., 2010, MNRAS, 409, 1631
Bonsor A., Wyatt M. C., 2012, MNRAS, 420, 2990
Borucki W. J. et al., 2011, ApJ, 736, 19
Brott I., Hauschildt P. H., 2005, in Turon C., O'Flaherty K. S., Perryman M., eds, The Three-Dimensional Universe with Gaia, ESA SP-576. ESA, Noordwijk, p. 565
Bryden G. et al., 2006, ApJ, 636, 1098
Bryden G. et al., 2009, ApJ, 705, 1226
Churcher L. J. et al., 2011, MNRAS, 417, 1715
Condon J. J., Cotton W. D., Greisen E. W., Yin Q. F., Perley R. A., Taylor G. B., Broderick J. J., 1998, AJ, 115, 1693
Eiroa C. et al., 2010, A&A, 518, L131
Fruchter A. S., Hook R. N., 2002, PASP, 114, 144
Golimowski D. A. et al., 2011, AJ, 142, 30
Gomes R., Levison H. F., Tsiganis K., Morbidelli A., 2005, Nat, 435, 466
Greaves J. S., Wyatt M. C., 2010, MNRAS, 404, 1944
Greaves J. S., Holland W. S., Jayawardhana R., Wyatt M. C., Dent W. R. F., 2004, MNRAS, 348, 1097
Greaves J. S., Fischer D. A., Wyatt M. C., 2006, MNRAS, 366, 283
Greenberg R., van Laerhoven C., 2012, MNRAS, 419, 429
Gregory P. C., Fischer D. A., 2010, MNRAS, 403, 731
Griffin M. et al., 2010, A&A, 518, L3
Hansen B. M. S., Murray N., 2012, ApJ, 751, 158
Hauschildt P. H., Baron E., 2009, A&A, 498, 981
Heng K., 2011, MNRAS, 415, 3365
Horner J., Jones B. W., 2010, Int. J. Astrobiol., 9, 273
Ida S., Lin D. N. C., 2010, ApJ, 719, 810
Kains N., Wyatt M. C., Greaves J. S., 2011, MNRAS, 414, 2486
Kelsall T. et al., 1998, ApJ, 508, 44
Kennedy G. M., Wyatt M. C., 2010, MNRAS, 405, 1253
Kennedy G. M. et al., 2012, MNRAS, 421, 2264
Kenyon S. J., Bromley B. C., 2010, ApJS, 188, 242
Kirsh D. R., Duncan M., Brasser R., Levison H. F., 2009, Icarus, 199, 197
Kóspál A., Ardila D. R., Moór A., Ábrahám P., 2009, ApJ, 700, L73
Krist J. E. et al., 2010, AJ, 140, 1051
Krivov A. V., 2010, Res. Astron. Astrophys., 10, 383
Lai D., Foucart F., Lin D. N. C., 2011, MNRAS, 412, 2790
Lawler S. M. et al., 2009, ApJ, 705, 89
Lebouteiller V., Barry D. J., Spoon H. W. W., Bernard-Salas J., Sloan G. C., Houck J. R., Weedman D. W., 2011, ApJS, 196, 8
Lecar M., Franklin F. A., Holman M. J., Murray N. J., 2001, ARA&A, 39, 581
Lestrade J.-F., Wyatt M. C., Bertoldi F., Menten K. M., Labaigt G., 2009, A&A, 506, 1455
Levison H. F., Morbidelli A., Tsiganis K., Nesvorný D., Gomes R., 2011, AJ, 142, 152
Lissauer J. J. et al., 2011, ApJS, 197, 8
Lovis C. et al., 2006, Nat, 441, 305
McNeil D. S., Nelson R. P., 2010, MNRAS, 401, 1691
Maldonado J., Eiroa C., Villaver E., Montesinos B., Mora A., 2012, A&A, 541, A40
Matthews B. C. et al., 2010, A&A, 518, L135

Mayor M., Queloz D., 1995, Nat, 378, 355

Mayor M., Udry S., Naef D., Pepe F., Queloz D., Santos N. C., Burnet M., 2004, A&A, 415, 391

Mayor M. et al., 2011, A&A, submitted (arXiv:1109.2497)

Melis C., Zuckerman B., Rhee J. H., Song I., 2010, ApJ, 717, L57

Moro-Martín A. et al., 2007, ApJ, 658, 1312

Moro-Martín A., Malhotra R., Bryden G., Rieke G. H., Su K. Y. L., Beichman C. A., Lawler S. M., 2010, ApJ, 717, 1123

Mustill A. J., Wyatt M. C., 2009, MNRAS, 399, 1403

Mustill A. J., Wyatt M. C., 2012, MNRAS, 419, 3074

Naoz S., Farr W. M., Lithwick Y., Rasio F. A., Teyssandier J., 2011, Nat, 473, 187

Ott S., 2010, in Mizumoto Y., Morita K. I., Ohishi M., eds, ASP Conf. Ser. Vol. 434, Astronomical Data Analysis Software and Systems XIX. Astron. Soc. Pac., San Francisco, p. 139

Payne M. J., Ford E. B., Wyatt M. C., Booth M., 2009, MNRAS, 393, 1219

Pepe F. et al., 2011, A&A, 534, A58

Phillips N. M., Greaves J. S., Dent W. R. F., Matthews B. C., Holland W. S., Wyatt M. C., Sibthorpe B., 2010, MNRAS, 403, 1089

Pilbratt G. L. et al., 2010, A&A, 518, L1

Poglitsch A. et al., 2010, A&A, 518, L2

Quillen A. C., 2006, MNRAS, 372, L14

Raymond S. N., Mandell A. M., Sigurdsson S., 2006, Sci, 313, 1413

Raymond S. N. et al., 2011, A&A, 530, A62

Raymond S. N. et al., 2012, A&A, in press (arXiv:1201.3622)

Rodriguez D. R., Zuckerman B., 2012, ApJ, 745, 147

Santos N. C. et al., 2004, A&A, 426, L19

Smith R., Wyatt M. C., Haniff C. A., 2009, A&A, 503, 265

Sousa S. G. et al., 2008, A&A, 487, 373

Sousa S. G., Santos N. C., Israelian G., Mayor M., Udry S., 2011, A&A, 533, A141

Stewart S. T., Leinhardt Z. M., 2009, ApJ, 691, L133

Tanner A., Beichman C., Bryden G., Lisse C., Lawler S., 2009, ApJ, 704, 109

Terquem C., Papaloizou J. C. B., 2007, ApJ, 654, 1110

Tinney C. G., Butler R. P., Jones H. R. A., Wittenmyer R. A., O'Toole S., Bailey J., Carter B. D., 2011, ApJ, 727, 103

Tremaine S., 1993, in Phillips J. A., Thorsett J. E., Kulkarni S. R., eds, ASP Conf. Ser. Vol. 36, Planets Around Pulsars. Astron. Soc. Pac., San Francisco, p. 335

Trilling D. E. et al., 2007, ApJ, 658, 1264

Trilling D. E. et al., 2008, ApJ, 674, 1086

Tsiganis K., Gomes R., Morbidelli A., Levison H. F., 2005, Nat, 435, 459

van Leeuwen F., 2007, A&A, 474, 653

Vican L., 2012, AJ, 143, 135

Vitense C., Krivov A. V., Löhne T., 2010, A&A, 520, A32

Vogt S., Butler R. P., Marcy G. W., Fischer D. A., Henry G. W., Laughlin G., Wright J. T., Johnson J. A., 2005, ApJ, 632, 638

Vogt S. et al., 2010, ApJ, 708, 1366

Weidenschilling S. J., 1977, Ap&SS, 51, 153

Wright N. J., Drake J. J., Mamajek E. E., Henry G. W., 2011, ApJ, 743, 48

Wyatt M. C., 2008, ARA&A, 46, 339

Wyatt M. C., Smith R., Greaves J. S., Beichman C. A., Bryden G., Lisse C. M., 2007a, ApJ, 658, 569

Wyatt M. C., Smith R., Su K. Y. L., Rieke G. H., Greaves J. S., Beichman C. A., Bryden G., 2007b, ApJ, 663, 365

Wyatt M. C., Clarke C. J., Greaves J. S., 2007c, MNRAS, 380, 1737

Zakamska N. L., Tremaine S., 2004, AJ, 128, 869

This paper has been typeset from a TEX/LATEX file prepared by the author.